PERGAMON

Journal of Structural Geology 25 (2003) 1525–1549

JOURNAL OF STRUCTURAL GEOLOGY

www.elsevier.com/locate/jsg

Strain partitioning of deformation mechanisms in limestones: examining the relationship of strain and anisotropy of magnetic susceptibility (AMS)

M.A. Evans[a,*], M.T. Lewchuk[b], R.D. Elmore[b]

[a]*Department of Geology and Planetary Science, University of Pittsburgh, Pittsburgh, PA 15260 USA*
[b]*School of Geology and Geophysics, University of Oklahoma, Norman, OK 73019 USA*

Received 1 September 2001; received in revised form 5 January 2002; accepted 11 June 2002

Abstract

In order to investigate the relationship between rock strain and anisotropy of magnetic susceptibility (AMS), strain partitioning and AMS analysis was conducted at 35 sites from two stratigraphically adjacent Paleozoic limestone units in the Patterson Creek and Wills Mountain anticlines in the central Appalachian orogen of West Virginia. In addition, anisotropy of anhysteretic remanent magnetization (AARM) was conducted on selected samples to examine the role of preferentially oriented magnetite on the AMS fabric.

Strain is partitioned into bed-normal shortening due to compaction solution strain ($\leq$35.0% shortening), bed-parallel shortening due to tectonic solution strain ($\leq$13.3% shortening), calcite twinning strain ($\leq$5.8% shortening), and grain-boundary-sliding ($\leq$26.7% shortening).

The AMS fabrics in the rocks were found to be a result of a complex interaction between rock lithology, deformation mechanisms, and strain magnitude. Although all the rocks have experienced the same deformation conditions, six different AMS fabrics are exhibited.

Each of the different AMS fabrics is a composite fabric resulting from the overprinting of three components: (1) an inherent primary depositional AMS fabric that is attributed to preferentially oriented phyllosilicates in the rock matrix; (2) a diagenetic and/or compaction AMS fabric formed during burial that is due to preferentially oriented phyllosilicates in solution structures and in the rock matrix; and (3) a tectonic AMS fabric that was imparted on the rocks by layer-parallel-shortening deformation prior to folding, and is also attributed to preferentially oriented phyllosilicates in solution structures and in the rock matrix, as well as twinning of ferroan calcite.

Keywords: Magnetic susceptibility; Strain partitioning; Limestone

1. Introduction

The anisotropy of magnetic susceptibility (AMS) is a physical property of rocks that is used for petrofabric and structural studies (see Hrouda, 1982; Borradaile 1988; Lowrie, 1989; Jackson and Tauxe, 1991; Rochette et al., 1992; Tarling and Hrouda, 1993; Borradaile and Henry, 1997 for reviews). The promise of AMS data is that it often shows a relationship with rock strain, both in terms of magnitude and fabric. Because it is relatively easy and fast to measure, as opposed to most methods of determining rock strain, many workers have attempted to directly correlate AMS to strain (e.g. Kligfield et al., 1982; Borradaile and Mothersill, 1984; Cogne and Perroud, 1987; Lüneburg et al., 1999; Hirt et al., 2000). However, success has been limited, and no reliable correlation has been established. This attempt at a correlation has been complicated by: (1) the inherent inhomogeneity of strain at the grain scale; (2) the fact that whole rock magnetic anisotropy is primarily a function of the diamagnetic and paramagnetic minerals of the rock matrix plus inhomogeneously distributed high susceptibility ferromagnetic grains; (3) the pre-deformation anisotropy fabric is generally unknown; and (4) the relationship between the final AMS shape fabric and multiple deformation events is difficult to establish.

Most studies to date that have attempted to relate AMS to strain have used finite strain (e.g. Borradaile and Mothersill, 1984; Lüneburg et al., 1999; Hirt et al., 2000), which measures the cumulative or end result of all strain events that a rock has experienced. However, at the grain scale, strain is distributed among one or more different deformation mechanisms. Each mechanism contributes differently to the finite strain and has a different role during the multiple events of the deformation history. For example, in

* Corresponding author. Tel./fax: +1-412-624-3914.
E-mail address: mae6@pitt.edu (M.A. Evans).

0191-8141/03/$ - see front matter © 2003 Elsevier Science Ltd. All rights reserved.
PII: S0191-8141(02)00186-4

foreland settings of an orogenic belt a typical series of deformation events includes: (1) compaction, (2) layer-parallel shortening, (3) folding, and (4) post-folding flattening. Any or all of these events contribute to the finite strain and involve different combinations of deformation mechanisms such as twinning, pressure solution, grain-boundary sliding, and fracturing. Hence, similar finite strains result from different strain paths with different suites of mechanisms.

The use of AMS to characterize the deformation is complicated by the fact that each deformation mechanism contributes to the AMS differently. The non-coaxial nature of deformation events and the potential of multiple deformation events complicates the relationship of strain to AMS even further. All susceptibility fabrics are really composite fabrics (Housen et al., 1993).

One approach to linking strain and magnetic susceptibility fabric is to examine how deformation mechanisms contribute to the anisotropy at the grain-scale during deformation. Although many workers have invoked grain-scale deformation in contributing to the development of AMS fabrics (e.g. Borradaile and Tarling, 1981; Borradaile, 1988, 1991; Jackson et al., 1989; Housen and van der Pluijm, 1991; Hrouda, 1993; Sun et al., 1993; Imaz et al., 2000), aside from general treatments by Borradaile (e.g. 1981, 1988) and Tarling and Hrouda (1993), few detailed examinations of the actual mineral deformation mechanisms exist (Borradaile and Tarling, 1984; Hirt et al., 1986).

Strain partitioning (Ramsay and Huber, 1983; Groshong et al., 1984; Wu, 1989; Evans and Dunne, 1991; Couzens et al., 1993; Onasch, 1994; Harrison and Onasch, 2000) is an effort to separate the finite strain into components caused by different deformation mechanisms. For example, in limestones deformed at low temperatures ($<200\,^{\circ}C$), finite strain may be partitioned into strain by: (1) pressure solution; (2) calcite twinning; (3) dislocation mechanisms; and (4) grain boundary sliding. By quantifying the contribution of each deformation mechanism, we can better understand which mechanism(s) contribute most to the magnetic grain distribution and orientation.

The purposes of this paper are: (1) to review deformation mechanisms of calcite and examine how these deformation mechanisms affect AMS fabrics in limestones; and (2) to show how strain partitioning can provide insight into the contribution of each deformation mechanism to the total AMS fabric. These purposes will be accomplished through a detailed study of AMS fabrics and strain in Paleozoic limestones from the central Appalachian Valley and Ridge province.

2. Geologic setting

Limestones from the Upper Silurian Tonoloway Formation and the stratigraphically adjacent Lower Devonian Helderberg Group (Head, 1974) were sampled from the macroscale Patterson Creek and the Wills Mountain anticlines in the central Appalachian Valley and Ridge province of northern West Virginia (Fig. 1). The area is part of a fold-and-thrust belt developed during the late Paleozoic Alleghanian orogeny (Rodgers, 1963, 1970; Gwinn 1964; Perry, 1978; Sacks and Secor, 1990). The stratigraphic section occurs in the middle of a roof sequence that overlies a blind duplex of Cambro–Ordovician carbonate rocks. The duplex is deformed by transport above a floor thrust in the Cambrian Waynesboro–Rome Formation (Gwinn 1964; Perry, 1978; Kulander and Dean, 1986; Wilson and Shumaker 1992; Dunne, 1996; Evans and Battles, 1999).

The two limestone formations were remagnetized during the Permian Kiaman event (Evans et al., 2000; Lewchuk et al., 2002) and have experienced the same macroscale deformation history as well as the same pressure–temperature–fluid conditions (Evans and Battles, 1999). The remagnetization is carried by magnetite and was acquired prior to- and early during folding deformation but the relationship to unfolding varied from site to site (Lewchuk et al., 2003). The site numbering system used in this study is the same as that used in Lewchuk at al. (2002) so that a direct comparison between the strain, rock magnetic and paleomagnetic data is possible.

Limestones of the Helderberg Group contain a wide range of carbonate lithologies including grainstones, wackestone, and carbonate mudstones (Dorobek and Read, 1986; Dorobek, 1987; Meyer and Dunne, 1990), but are dominated by coarse-grained lithologies. In contrast, the Tonoloway Formation is dominated by fine-grained lithologies such as carbonate mudstone, although coarser grained rocks such as wackestones and occasional packstones and grainstones are present. In outcrop, the rocks of both formations exhibit common to pervasive bed-parallel stylolites that are spaced on the order of centimeters to tens of centimeters. Bed-normal stylolites are rare, occurring locally within individual beds.

3. Methodology

3.1. Sampling, petrography and strain

For the magnetic sampling, 8–12 core plugs were taken at each of 20 sites located in two transects across the Patterson Creek anticline and a further 15 sites along two transects across the Wills Mountain Anticline (Fig. 1). Oriented block samples were collected at each site from within the same layer cored for magnetic samples. Block samples were taken as close as possible to the core holes and usually incorporated the cored rock.

Three mutually perpendicular thin sections were cut from each block sample and polished to 0.05 μm alumina. They were examined by optical and reflectance petrographic methods in transmitted plane and polarized light to determine mineralogy and characterize the structures and

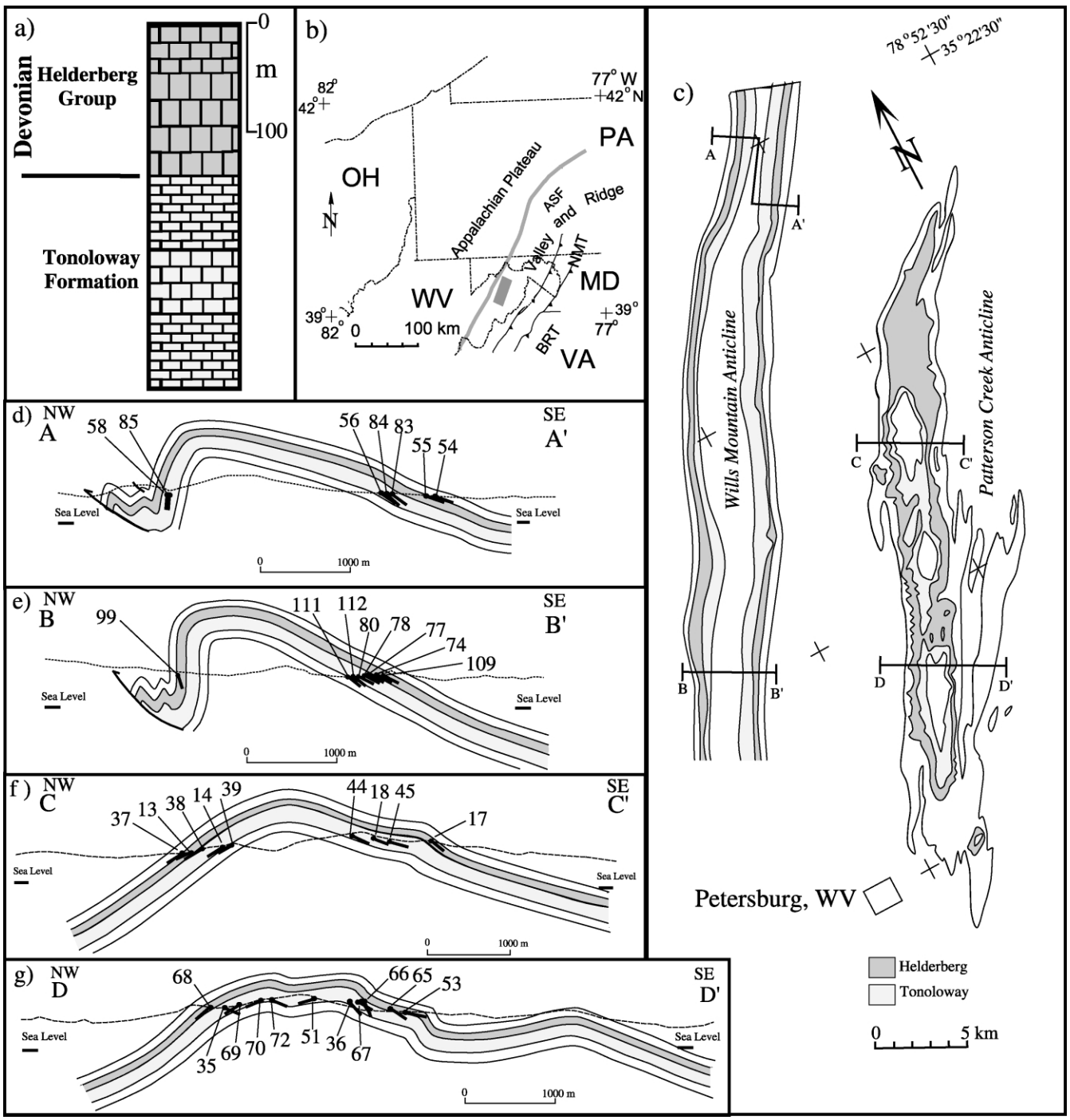

Fig. 1. (a) Stratigraphic column showing limestone units sampled for this study, (b) regional map showing location of sampled fold (shaded box), (c) geologic map of the Patterson Creek and Wills Mt. anticlines showing location of sampling transects, and (d)–(g) cross-sections showing sample sites and bedding dips. ASF = Appalachian Structural Front. Numbers are sample sites and ball and stick diagrams are site locations and bedding dip.

hence, infer deformation mechanisms that were operative in the rock. Several samples with pressure solution structures were examined using a scanning electron microscope (SEM) to characterize the geometry and mineralogy in more detail. One thin section from each site was stained with alizaine red S and potassium ferricyanide (Dickson, 1966) to distinguish between ferroan and non-ferroan carbonate phases.

3.2. Anisotropy of magnetic susceptibility (AMS)

Magnetic susceptibility is a physical property of solids and represents the capacity of the material to be magnetized in a given magnetic field. In anisotropic materials, the magnetic susceptibility (K) can be described as a second-rank tensor that relates the applied magnetic field (H) to an induced magnetization (M) in a sample by $M_{ij} = K_{ij}H_j$. The

shape of the susceptibility ellipsoid is defined by three principle axes ($K_{max} > K_{int} > K_{min}$) whose orientations correspond to the eigenvectors of the susceptibility tensors. AMS ellipsoids may be analyzed similarly to traditional fabrics or shape characteristics. For example, K_{max}/K_{int} (magnetic lineation) vs. K_{int}/K_{min} (magnetic foliation) may be plotted on Flinn-type plots to assess the shape and degree of fabric development. Another presentation for AMS measurements is the Jelínek plot (Jelínek, 1981; Hrouda, 1982) where P_j, the degree of fabric development or strain is plotted directly on the X-axis with increasing fabric intensity to the right. T_j, the shape parameter is plotted on the Y-axis with oblate fabrics having T_j values greater than zero (to a maximum of $+1$) and prolate fabrics less than zero (to a minimum of -1). The principal axes of the ellipsoid may also by displayed on stereonet projections to investigate geometric relationships.

Anisotropy of magnetic susceptibility (AMS) measurements were made on at least 2–18 specimens (usually >10) from each of 11 sites in the Helderberg Group and 24 sites in the Tonoloway Formation using a Sapphire Instruments (SI-2B) susceptibility meter. Only specimens with close to ideal shapes (right cylinders with a height of approximately 0.9 of the diameter) were used to minimize effects due to specimen shape. Each specimen was measured twice in each of six positions to generate the AMS tensor using the AMS package for the SI2B written by G. Borradaile (personal communication, 2000). The data are summarized in Table 1.

3.3. Anisotropy of anhysteretic remanent magnetization (AARM)

In order to evaluate the contribution of magnetite to the AMS response, we measured the anisotropy of anhysteretic remanent magnetization (AARM) on selected samples. Unlike AMS, AARM yields the magnetic anisotropy that resides only in magnetite and other ferromagnetic minerals (Jackson, 1991). The AARM was imparted using a modified Schondstedt AF demagnetizer with a 0.1 mT DC bias field and peak fields of 100 mT. Measurements were made in eight different orientations on a 3 axis 2G cryogenic magnetometer. The data are summarized in Table 2.

4. AMS and strain

4.1. Minerals contributing to the AMS

Magnetic anisotropy is the result of the contributions from the anisotropy of all magnetic phases (diamagnetic, paramagnetic, and ferromagnetic) that compose the rock. In addition, the total rock magnetic fabric can reflect a shape anisotropy caused by the alignment of mineral grains and/or a crystalline anisotropy resulting from the alignment of crystal axes (Tarling and Hrouda, 1993). Although ferromagnetic minerals have a much higher susceptibility, the contribution of the far more abundant paramagnetic or diamagnetic minerals can exceed that of the ferromagnetic minerals (Rochette, 1987; Hrouda et al., 1988; Henry, 1989; Jackson et al., 1989; Borradaile and Sarvas, 1990; Housen and van der Pluijm, 1990). In some cases, interspecimen variation in ferromagnetic grain content may result in significant variations in the shape of the AMS ellipsoid (Borradaile, 1987). Generally, susceptibilities greater than 5000×10^{-6} SI are assumed to indicate that the ferromagnetic minerals are dominating the signal, whereas susceptibilities less than 500×10^{-6} SI indicate that paramagnetic minerals are controlling the signal (Tarling and Hrouda, 1993). All but two samples evaluated for this study have susceptibilities less than 500×10^{-6} SI (Table 1), so we assume that the ferromagnetic contribution is low.

The polymineralic nature of most rocks adds further complications. Because AMS simultaneously measures the susceptibility of all minerals in a rock, it will combine the contribution of minerals with different orientations. In such situations, the observed AMS does not accurately reflect the preferred orientation of any single mineral, but instead reflects the summed contribution of all grains.

Although the limestones examined in this study are nearly monominerallic (Table 2), with calcite as the primary mineral, they contain ferromagnetic minerals and phyllosilicates that all contribute to the magnetic susceptibility.

4.1.1. Calcite

Calcite forms the bulk of the rock mineralogy, generally constituting $>96\%$ of the rock, with the remainder being quartz, dolomite, or selvage zone material. In three samples calcite constitute $<90\%$ of the rock (Table 2).

Calcite has a uniaxial diamagnetic susceptibility anisotropy prolate about the c-axis (Owens and Bamford, 1976) (Fig. 2). However, calcite becomes paramagnetic with the addition of Fe^{2+} ions (Rochette, 1988; Rochette et al., 1992) and can form an inverse AMS fabric. An inverse magnetic fabric is defined by a K_{max} direction that is parallel to the tectonic shortening direction and a K_{min} that is normal to the tectonic shortening direction (Rochette, 1988; Ihmlé et al., 1989). Nearly all limestones sampled for this study can be classified as ferroan from staining and microprobe work done on the Helderberg limestones by Dorobek (1987).

4.1.2. Ferromagnetic minerals

Thin section petrography and SEM analysis were used to characterize the distribution of iron oxide minerals, particularly magnetite, in the Tonoloway and Helderberg limestones. Iron oxide inferred to be magnetite is found in four modes: (1) irregular or blocky shaped multidomain (MD) size and pseudosingle domain (PSD) size (Butler and Banerjee, 1975) grains randomly scattered in the matrix; (2) pseudoframboids (spherical cluster of single domain (SD) size grains) randomly distributed in the matrix or concentrated in solution structures; (3) SD-size sub-euhedral crystals within solution structures (Fig. 3); and (4) as

Table 1
Magnitudes and orientations of the principle axes of the site means of the AMS ellipsoid in geographic coordinates

Site	Formation	Strike[a]	Dip[a]	n/N[b]	K_{min}[c]	D_{min}[d]	I_{min}[d]	K_{int}[c]	D_{int}[d]	I_{int}[d]	K_{max}[c]	D_{max}[d]	I_{max}[d]	Mean k_{bulk} ($\times 10^{-6}$)	P_j	T_j
13	Helderberg	202	30	2/2	0.982	144	57	1.003	329	31	1.014	333	65	59	1.03	0.33
14	Tonoloway	201	33	2/2	0.966	117	44	1.005	346	36	1.030	235	25	233	1.07	0.23
17	Helderberg	022	45	5/5	0.982	299	49	1.005	119	43	1.011	133	48	141	1.03	0.60
18	Tonoloway	032	23	2/2	0.946	309	70	1.015	153	19	1.041	060	8	259	1.10	0.47
35	Tonoloway	052	32	14/14	0.961	113	44	1.010	275	45	1.028	303	45	54	1.07	0.46
36	Tonoloway	022	28	10/10	0.914	295	55	1.027	149	30	1.063	049	16	484	1.17	0.54
37	Helderberg	204	33	14/14	0.966	114	57	1.002	347	54	1.032	289	32	93	1.07	0.06
38	Tonoloway	204	40	13/13	0.951	111	51	1.010	233	26	1.040	332	31	406	1.10	0.30
39	Tonoloway	206	35	13/15	0.932	115	57	1.023	328	29	1.047	230	18	259	1.13	0.60
44	Tonoloway	032	30	11/11	0.906	295	63	1.029	186	11	1.071	095	25	91	1.19	0.54
45	Tonoloway	012	25	11/11	0.955	340	73	1.007	212	26	1.038	139	26	50	1.09	0.29
51	Tonoloway	232	18	14/14	0.947	156	75	1.010	031	9	1.044	299	13	537	1.10	0.33
53	Helderberg	017	16	17/18	0.972	302	73	1.003	070	20	1.025	142	24	108	1.06	0.18
54	Helderberg	018	22	16/16	0.952	298	73	0.994	108	18	1.055	193	8	175	1.11	−0.16
55	Helderberg	018	22	11/13	0.976	295	79	0.999	084	42	1.025	167	16	73	1.05	0.02
56	Tonoloway	030	38	13/16	0.958	303	54	1.012	121	36	1.030	141	31	167	1.08	0.52
58	Tonoloway	222	84	21/21	0.966	073	62	1.004	261	86	1.030	324	81	56	1.07	0.20
65	Helderberg	042	37	13/14	0.976	306	55	1.004	094	32	1.019	180	24	215	1.04	0.37
66	Tonoloway	029	70	16/17	0.948	301	48	0.996	135	41	1.058	043	15	48	1.12	−0.12
67	Tonoloway	032	57	13/13	0.979	125	65	1.001	326	24	1.019	253	16	54	1.04	0.12
68	Helderberg	212	44	14/14	0.977	127	44	1.006	276	42	1.016	009	26	98	1.04	0.48
69	Tonoloway	222	34	10/15	0.979	134	66	1.002	323	26	1.019	272	19	303	1.04	0.17
70	Tonoloway	222	27	15/15	0.961	134	62	1.007	023	20	1.032	298	27	85	1.08	0.32
72	Tonoloway	045	37	12/12	0.983	121	37	0.998	303	54	1.019	219	26	157	1.04	−0.12
74	Helderberg	032	50	9/9	0.997	316	54	0.985	078	39	1.037	191	24	103	1.07	−0.72
77	Tonoloway	030	44	7/7	0.977	026	76	0.986	318	65	1.037	190	13	207	1.07	−0.68
78	Tonoloway	029	45	6/6	0.961	050	81	0.980	285	46	1.060	190	10	584	1.11	−0.61
80	Tonoloway	027	45	8/8	0.970	104	60	0.993	306	29	1.036	210	12	86	1.07	−0.29
83	Tonoloway	036	40	8/9	0.971	307	56	0.994	104	32	1.034	200	11	215	1.07	−0.26
84	Tonoloway	031	45	8/8	0.971	303	52	1.006	130	37	1.022	128	53	294	1.05	0.36
85	Tonoloway	222	83	14/14	0.975	121	25	0.999	279	67	1.026	015	51	325	1.05	−0.17
99	Helderberg	027	62	12/12	0.983	140	60	0.999	292	27	1.017	023	18	89	1.04	−0.04
109	Helderberg	047	25	12/12	0.960	332	78	0.989	065	73	1.052	185	11	73	1.10	−0.40
111	Tonoloway	030	36	9/9	0.961	297	51	0.993	101	38	1.047	196	15	73	1.09	−0.22
112	Tonoloway	034	39	8/8	0.966	307	46	0.996	112	44	1.038	212	13	66	1.08	−0.20

[a] Strike and dip are in right-hand-rule format.
[b] n/N is number of samples used versus number of samples taken.
[c] K_{min}, K_{int}, and K_{max} are lengths of the AMS ellipsoid axes.
[d] D_{min}, I_{min}, D_{int}, I_{int}, D_{max}, and I_{max} are declinations and inclinations for AMS ellipsoid axes.

irregular-shaped grains found in fossil fragments and pellets. The magnetite is both detrital and authigenic in origin. Although all rocks in this study were remagnetized during the Permian (Kiaman), the timing of the original chemical remagnetization is generally pre- to syn-folding (Lewchuk et al., 2002). However, Lewchuk et al. (2003) also show that for the same samples examined in this study, there is a correlation between increasing total solution strain and degree of syn-folding character of rock magnetization. This suggests that during the solution process, existing magnetite was realigned, and/or new magnetite grains were grown.

All the observed MD, PSD, and SD magnetite grains seen in thin section and in SEM images are nearly equidimensional. However, because of the strong magnetic susceptibility anisotropy of magnetite crystals, even slightly irregular grains will have a strong magnetic anisotropy. In addition, the size of the magnetite grains will affect the susceptibility response. Elongate MD grains will have both the AMS and AARM k_{max} directions parallel to the long axis of the grain. However, elongate SD grains have the AARM k_{max} axis parallel to the long axis of the grain, whereas AMS K_{max} axis is normal to the long axis of the grain (Jackson, 1991).

4.1.3. Phyllosilicates

Phyllosilicates are common constituents of limestones, particularly in finer-grained, mudstones and wackstones (Marshak and Engelder, 1985). They are typically disseminated between calcite grains of the rock matrix. Where grain-to-grain or stylolitic pressure solution has occurred, they are concentrated in the 'selvage zones' where they have accumulated from either the dissolution of the host rock and/or precipitation during pressure solution. Chlorite,

Table 2
Orientations of the principle axes of the specimen AARM ellipsoids in geographic coordinates

Site	Formation	D_{min}[a]	I_{min}[a]	D_{int}[a]	I_{int}[a]	D_{max}[a]	I_{max}[a]	% Anisotropy[b]	k_{max}/k_{int}	k_{int}/k_{min}
36a	Tonoloway	305	52	133	37	40	4	10.647	1.032	1.080
36b	Tonoloway	295	52	139	36	41	12	11.968	1.034	1.094
36c	Tonoloway	297	60	131	29	38	6	19.300	1.077	1.131
37	Helderberg	109	74	220	6	312	15	8.487	1.032	1.056
53a	Helderberg	13	80	273	2	182	10	8.531	1.014	1.077
53b	Helderberg	277	68	132	18	38	11	12.487	1.026	1.110
56a	Tonoloway	301	70	75	15	169	14	5.891	1.038	1.022
56b	Tonoloway	306	67	106	22	199	8	7.955	1.046	1.035
65a	Helderberg	299	46	167	33	59	26	9.858	1.026	1.079
65b	Helderberg	300	50	171	28	66	26	5.822	1.008	1.053
66a	Tonoloway	298	28	116	62	207	1	5.429	1.026	1.029
66b	Tonoloway	300	39	97	49	201	12	5.381	1.026	1.028
66c	Tonoloway	303	34	130	56	35	4	10.943	1.022	1.096
66d	Tonoloway	284	40	18	5	113	49	4.785	1.021	1.028
69a	Tonoloway	135	61	344	26	248	13	5.089	1.011	1.041
69b	Tonoloway	140	69	9	14	275	15	4.520	1.020	1.026
70a	Tonoloway	135	52	319	37	35	8	6.794	1.032	1.038
70b	Tonoloway	288	38	113	49	28	12	5.330	1.035	1.018
72a	Tonoloway	133	42	332	47	232	10	4.775	1.011	1.038
72b	Tonoloway	125	35	334	51	225	15	5.210	1.025	1.028
74	Helderberg	50	48	306	13	205	39	23.122	1.103	1.147
77	Tonoloway	357	75	95	2	186	15	20.463	1.217	1.148
80	Tonoloway	87	54	322	25	215	24	8.284	1.039	1.046
84	Tonoloway	13	43	153	40	261	21	21.829	1.101	1.133
99	Helderberg	40	32	134	6	233	57	9.847	1.070	1.029
109	Helderberg	70	60	309	17	211	24	19.758	1.174	1.024
111	Tonoloway	72	40	309	33	195	33	19.929	1.066	1.154
112	Tonoloway	329	6	230	55	63	35	9.699	1.088	1.009

[a] D_{min}, I_{min}, D_{int}, I_{int}, D_{max}, and I_{max} are declinations and inclinations for AARM ellipsoid axes.
[b] % Anisotropy $= (k_{max} - k_{min})/((k_{max} + k_{int} + k_{min})/3) \times 100$.

micas, and other paramagnetic phyllosilicates possess an intrinsic oblate magnetic anisotropy, with the K_{min} axis normal to the crystallographic basal plane, and the corresponding K_{max} and K_{int} axes parallel to the plane and nearly equal in magnitude (Fig. 3a) (Hrouda, 1982; Rochette et al., 1992; Borradaile and Werner, 1994).

4.2. Models

Various theoretical models have been proposed to address the relationship between AMS and strain: passive, line/plane, ductile, and viscous (see Tarling and Hrouda (1993) and Hrouda (1993) for reviews). Although these models provide a convenient, mathematical means of evaluating the relationship between rock strain and anisotropy, none account for the actual deformation mechanisms of rocks. Consequently, these models have had little success when applied to rocks (Borradaile, 1988; Hrouda, 1993). In reality, rock strain is dependent on the mineralogy, grain size, pressure, temperature, and strain rate, which in turn determine the operative deformation mechanisms. The mechanisms control the post-deformation distribution and orientation of grains that contribute to the magnetic fabric.

5. Calcite deformation mechanisms

To understand the mechanical behavior of the limestones in this study, deformation mechanism maps (Frost and Ashby, 1982) were constructed for calcite at two different grain sizes. The 6 μm deformation mechanism map (Fig. 4a) is used to represent the mechanical behavior of micritic material that dominates the mudstones and the wackestones, while the 400 μm deformation mechanism map (Fig. 4b) is used to represent the behavior of coarser grained material of the packstones and the grainstones. The deformation mechanism maps only show which mechanism is likely to account for the most strain. The label in any particular field does not mean that no other mechanism or process is active, but it does mean that the microstructural development should be dominated by that labeled mechanism.

Many rocks, however, have a distribution of grain sizes. These distributed grain size systems are stronger at low stresses, while two or more mechanisms may contribute significantly to the total strain (Freeman and Ferguson, 1986). At a constant stress, the smallest grains deform fastest and the largest grains deform slowest. In addition, grain-scale stresses may vary widely when the grain size variation is large, such that the greatest local stresses may be an order of magnitude greater than the applied stress.

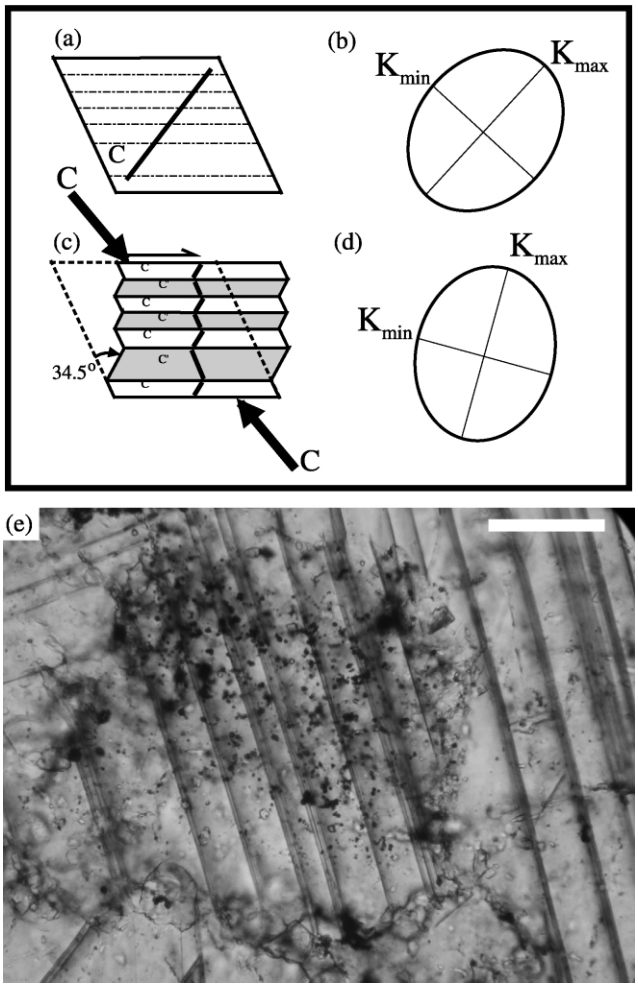

Fig. 2. (a) Relationship of c-axis is a calcite grain with potential e-twin planes. (b) Shape of the susceptibility ellipse for the undeformed grain shown in (a). K_{max} is parallel to the c-axis. (c) Calcite grain after significant mechanical twinning showing the reorientation of the c-axis within the twinned material. The arrows labeled 'C' are the compression direction responsible for twinning. Note that the c-axes within the twinned material are reoriented toward the compression axis. (d) Susceptibility ellipse for the calcite grain after twinning. Note that the K_{max} direction rotates toward the compression axis giving an 'inverse' pattern. (e) Calcite grain in limestone showing twins. Dark spots are iron oxide grains in an echinoid core of the overgrown grain. Scale bar is 50 microns.

Therefore, in this study we have divided our samples into two groups: mudstones and wackstones where deformation was controlled by micrite-size grains; and packstones and grainstones where deformation was controlled by coarse (generally >100 μm) grains.

In rocks that have two minerals, such as an arenaceous limestone or a dolomitic limestone, the compositionally dominant mineral will control the strain rate of the aggregate. For this study, calcite dominates compositionally (Table 2), so calcite is interpreted to have controlled the rock deformation. In the following sections, each calcite deformation mechanism is examined for its effect on bulk rock magnetic anisotropy.

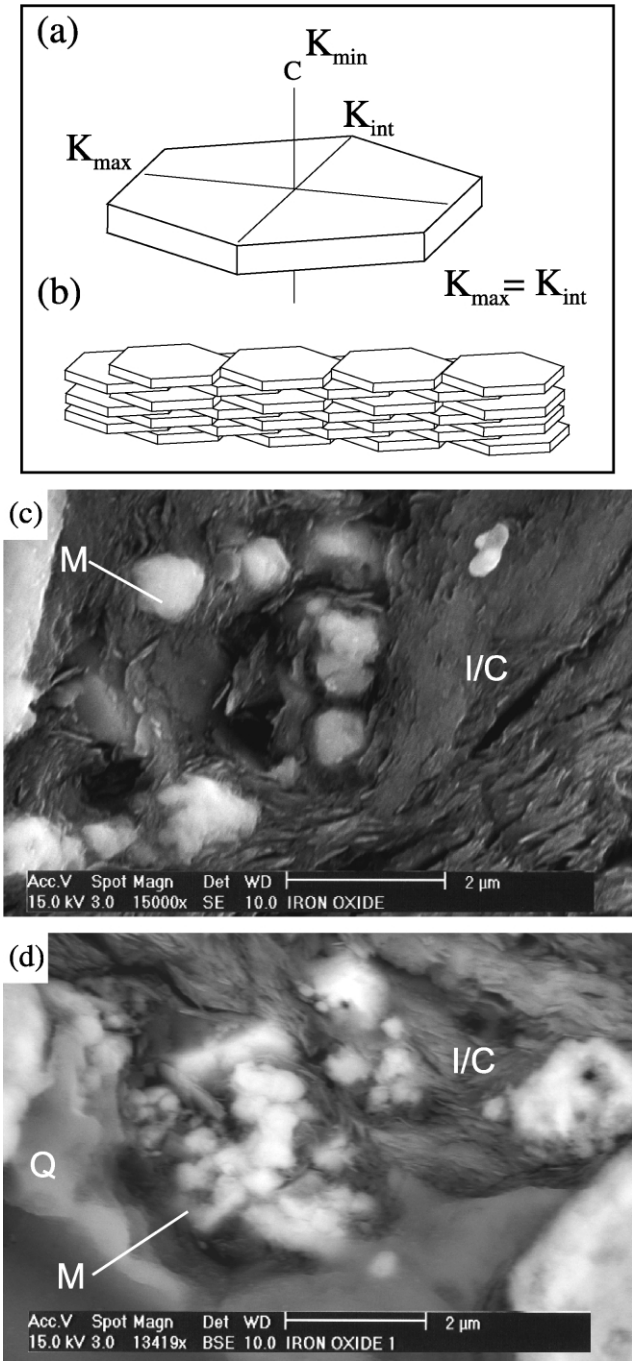

Fig. 3. (a) Typical phyllosilicate crystal showing the susceptibility axes. (b) Sketch of alignment of phyllosilicates within a pressure solution zone. (c) and (d) Scanning Electron Microscope images of selvedge zones within stylolites. Note the alignment of phyllosilicates (I/C), here illite and chlorite. Also shown are magnetite (M) crystals that are interpreted to be new grains grown within the stylolite zones during pressure solution deformation. Q is a pressure-solved quartz grain.

5.1. Pressure solution

Pressure solution structures in calcite-rich limestones are usually described as either stylolitic, where transgranular pressure solution transects the whole rock in the form of stylolites (Fig. 5a); or grain-to-grain (Fig. 5b) (Bathurst,

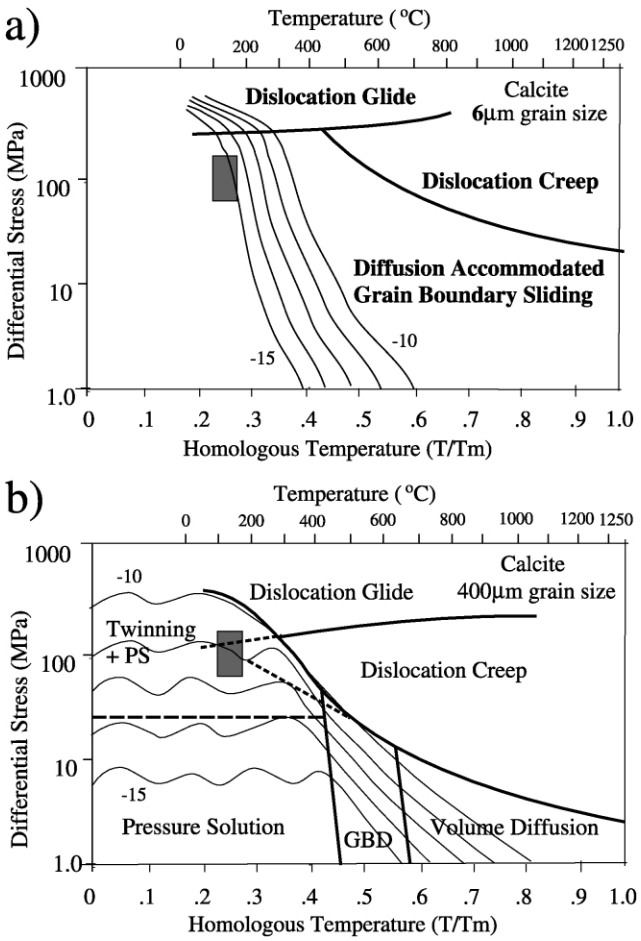

Fig. 4. Deformation mechanism maps for calcite at (a) 6 micron grain size and (b) 400 micron grain size. The maps were constructed using published constitutive equations and flow laws for calcite (Rutter, 1974, 1976; Schmid et al., 1977; Schmid, 1982a,b). Shaded rectangle represents deformation conditions for the rocks in the study area based on fluid inclusion data from Evans and Battles (1999).

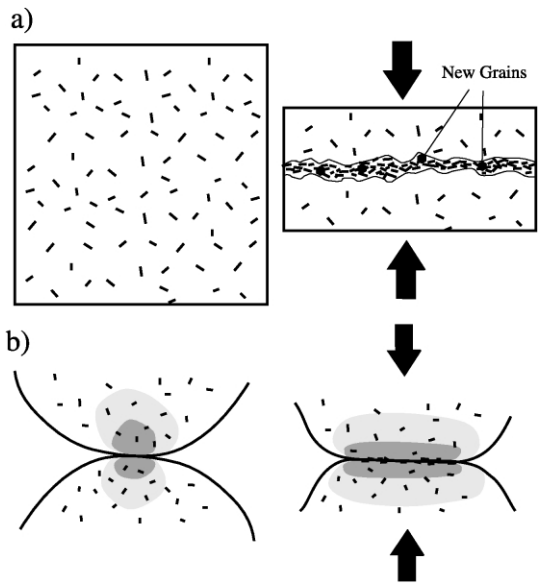

Fig. 5. (a) Schematic diagram showing pressure solution of a mudstone rock. (b) Schematic of grain-to-grain pressure solution in grainstone rock. Shaded zones represent decreasing stress away from the point of grain contact. In both cases volume loss occurs and 'insoluble' material is concentrated at solution sites. 'Survivor' grains may rotate into the solution structure and new grains may grow. Ferromagnetic grains are represented as small rectangles in host grains.

1971; see Groshong (1988) and Passchier and Trouw (1996) for reviews of pressure solution phenomena). The difference is only that of scale, as the mechanism is the same.

Pressure solution deformation may affect magnetic anisotropy in several ways. First, pressure solution destroys pre-existing minerals, thereby altering the original susceptibility of the rock. Second, new minerals may precipitate at solution sites. In this study, micron-size magnetite, and chlorite are interpreted to have formed along stylolites (Fig. 3c and d). Third, as adjacent calcite is dissolved, rotation of both ferromagnetic and paramagnetic mineral grains at solution sites may contribute to magnetic anisotropy fabrics (Borradaile and Tarling, 1981; Borradaile, 1988; Tarling and Hrouda, 1993; Housen et al., 1993; Imaz et al., 2000). In particular, chlorite is very paramagnetic and may make a significant contribution to magnetic susceptibility fabrics (Housen and van der Pluijm, 1990). In the Tonoloway and Helderberg, mixed chlorite and illite are highly aligned within the pressure solution zones (Fig. 3c and d). Since phyllosilicate alignment is only along the basal plane, and the susceptibility axes within that plane are nearly equal, this preferred orientation will produce girdle distributions of the AMS K_{int} and K_{max} values in the average plane of the stylolite or grain contact solution site.

Pressure solution of all minerals within a solution structure is enhanced by the presence of clays (Heald, 1956; Wanless, 1979; Marshak and Engelder, 1985). Therefore, limestones with greater clay content will also have a larger amount of strain due to pressure solution (Meyer and Dunne, 1990) and a greater contribution to the AMS fabric by pressure solution is expected.

5.2. Deformation twinning

The most common deformation mechanism in coarse calcite is mechanical twinning (Burkhard, 1993). Since the critical resolved shear stress for twinning is very low (about 10 MPa), twinning is nearly pervasive in limestones even when subjected to low tectonic differential stress (Craddock and van der Pluijm, 1989). In this study, twins are generally found in grains greater than 30–40 μm in size and become more common in larger grains. Calcite contains three potential deformation twin planes that involve a lattice rotation of 34.5° (see Burkhard (1993) for a review; Evans and Groshong, 1994). In this study, individual twins are 0.5 to over 10 μm thick (Fig. 2b) and individual calcite grains may have up to 15% twinned material along one, two, or three twin sets. Twinning may contribute to AMS fabric in several ways. First, mechanical twinning reorients the crystal c-axis and the K_{max} axis within the twinned material

of a calcite grain toward the maximum shortening direction (Fig. 2a). Therefore, the bulk grain magnetic anisotropy will also be rotated to a lesser degree toward the shortening direction. In an aggregate of randomly oriented grains, c-axes generally rotate toward the shortening axis, resulting in an 'inverse' magnetic fabric with the K_{max} direction parallel to the maximum shortening direction. In addition, twinning results in whole-grain distortion. Small magnetic particles on the grain boundaries and within twinned material will also rotate, but toward the plane of flattening.

5.3. Diffusion-accommodated grain boundary sliding

Fine-grained limestones of micrite-sized (1–10 μm) particles deform plastically as shown by deformed markers such as pellets. The deformation is accomplished by grain-boundary sliding, where grains undergo a neighbor switching process (Fig. 6) accomplished by diffusion at grain boundaries (Coble creep) (Raj and Ashby, 1971; Schmid et al., 1977; Raj, 1982). In this process, a rock accumulates considerable strain, while the grains themselves exhibit no obvious deformation or preferred orientation (Burkhard, 1990).

In terms of magnetic anisotropy, because grain shape is unchanged and grains are not aligned, rocks that experience grain boundary sliding should exhibit no magnetic anisotropy due to strain. Similarly, small rigid paramagnetic or ferromagnetic particles that are located within host grains will not undergo any significant rigid-body rotation because internal grain distortion is lacking (Fig. 6). However, inequant rigid particles located at host grain boundaries will passively rotate into the shortening direction (Fig. 6).

Given paramagnetic or ferromagnetic grains that are as large, or larger than the population of host grains, two cases must be considered. Under conditions of pure shear deformation, equant grains will not exhibit significant rigid-body rotation due to the motion of the adjacent calcite grains (Fig. 7a). However, for elongate or platy grains (such as phyllosilicates), rigid body rotation occurs (Fig. 7b). Simple shear deformation, on the other hand, will result in rigid grain rotation for both equant and inequant grain shapes (Fig. 7a and b). Large pure shear and/or simple shear

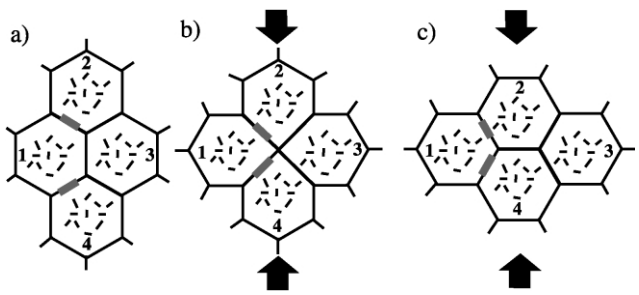

Fig. 6. Grain boundary sliding by neighbor switching. Switching of grain configuration (a) before, (b) during, and (c) after deformation. Ferromagnetic grains are represented as small rectangles in host grains and as large rectangles on grain boundaries.

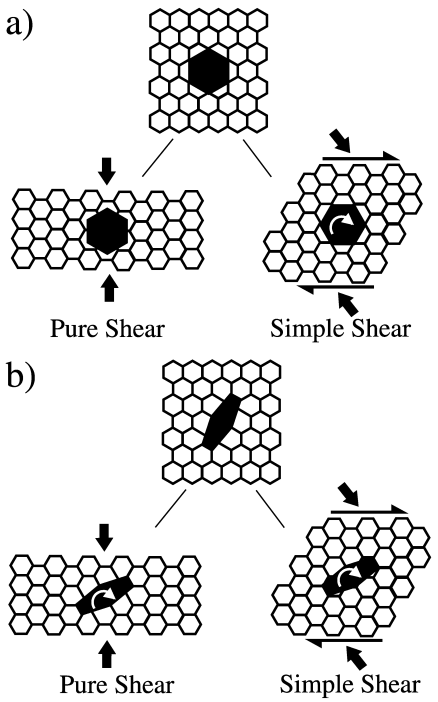

Fig. 7. (a) Effect of grain-boundary-sliding during pure shear and simple shear on large ferromagnetic grains that are equant (a) and inequant (b).

strains will result in aligned disseminated paramagnetic and ferromagnetic grains, which contribute to the AMS fabric.

5.4. Dislocation mechanisms

As deformation temperatures near 200 °C, dislocation glide is favored in larger calcite grains (Fig. 4) (Schmid, 1982a,b). This mechanism distorts the calcite grain lattice and is recognized by bent twins and undulose extinction (Fig. 8). Calcite grains undergoing distortion by dislocation mechanisms will flatten normal to the shortening direction, thereby resulting in a general rotation of c-axes (K_{max} axes) into the shortening plane. This rotation tends to counteract the opposite sense of c-axis rotation from twinning. Rigid ferromagnetic grains within, or on the boundaries of, calcite grains undergoing dislocation glide may passively rotate as the grain aggregate distorts during deformation (Fig. 8). Yet, at the pressure and temperature conditions for rocks in the study area, twinning dominates over a minor amount of dislocation glide.

6. Strain partitioning

For each sample, strain partitioning was done to quantify the contribution of each deformation mechanism (Tables 3–5, Figs. 9 and 10).

6.1. Pressure solution strain

Several techniques may be used to estimate volume loss

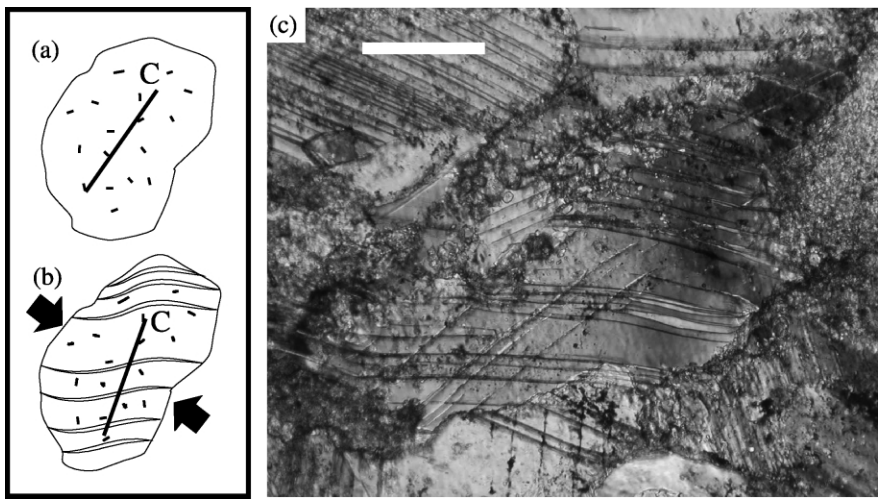

Fig. 8. Schematic diagram showing the effect of dislocation mechanisms on a calcite grain. (a) Undistorted calcite grain with c-axis (C) and ferromagnetic inclusions (short lines). With grain distortion by dislocation mechanisms (b) the c-axis rotates away from the shortening direction, as does any inclusion within the grain. (c) Photomicrograph showing effect of dislocation on a calcite grain with twins. Note bent twins. Scale bar is 50 microns.

due to pressure solution. For stylolites, stylolite amplitude (Stockdale, 1926; Bodou, 1976; Silbey and Blatt, 1976; Smart et al., 1997) yields a minimum estimate of volume loss parallel to the stylolite teeth. Alternatively, concentrations of relatively insoluble mineral grains in the selvage (pyrite, quartz, or dolomite) may be used to determine volume loss (Heald, 1956; Silbey and Blatt, 1976). In this study, the distribution of authigenic quartz in the matrix was compared with the concentration of quartz in stylolite zones. Up to 10 scanlines were made across a photomicrograph mosaic, and the distribution of quartz in the matrix was compared with that in the stylolite zone (in microns per microns of scan length). This volume-loss determination compared favorably with that determined by stylolite amplitude measurements for the same stylolite. However, this method only gives a minimum value for volume loss because the quartz also shows evidence for dissolution within the stylolites. Therefore, where authigenic quartz was present, both methods were used, where authigenic quartz was lacking, only stylolite amplitude was used. In most samples, we were able to partition the pressure solution strain into compaction versus tectonic shortening. Compactional solution surfaces are parallel to bedding (Fig. 11a), while tectonic solution surfaces are generally normal (Fig. 11b) or, more rarely, at an acute angle to bedding. Many samples exhibit both compaction and tectonic pressure solution (Fig. 11c).

6.1.1. Compaction pressure solution

Nearly all samples exhibit compactional solution in the form of macroscopic bed-parallel stylolites and/or grain-to-grain penetration. Individual stylolites have amplitudes of 0.2–3.0 mm, which provides a minimum estimate of bed-normal volume loss. Total minimum compaction-related volume loss per thin section ranges from 1.0 to 35.0% (Table 3, Figs. 9 and 10) and is quite variable from site to site. This variability may be attributed to the variable clay content of the limestones. In all cases, stylolitic teeth are bed-normal, indicating bed-normal compaction which is assumed to be primarily a pre-folding vertical compaction.

6.1.2. Tectonic pressure solution

Tectonic solution is manifested as bed-normal stylolites with amplitudes of 0.2–1.0 mm. They occur in half of the samples and where present, only one or two occur per thin section. They are similarly uncommon in outcrop, although they are locally common in small folds (Markley and Wojtal, 1996). These stylolites typically account for less than 4.0% layer-parallel shortening due to volume loss but may locally reach 13.3% (Table 3, Figs. 9 and 10). Where found in outcrop, they strike 036° ± 7° with teeth orthogonal to the stylolite surface, indicating maximum shortening directed 306° ± 7° (Fig. 12b). The bed-normal geometry of the stylolites indicates that intrabed shear and passive rotation of prefolding stylolites was not a factor (Meyer and Dunne, 1990; Markley and Wojtal, 1996). Only site 38 has subvertical stylolites interpreted to be post-folding, with 3.0% shortening due to solution.

6.2. Twinning strain

We used the calcite strain gage technique (Groshong, 1972, 1974; Evans and Groshong, 1994) to calculate twinning strains in 20–30 grains from each of two-mutually perpendicular thin sections (Table 4, Figs. 9 and 10). We were able to obtain data from 11 samples of coarse-grained packstones and grainstones, while only four samples of mudstones and wackestones contained enough coarse calcite grains for analysis. Twin shortening ranges from 0.46 to 5.79% (Table 4) but does not correlate to structural position on folds. In all cases, the maximum shortening direction is within ±5° of bedding (Fig. 12b), which we

Table 3
Summary of lithology and strain data

Site	Formation	Lithology[a]	Calcite >10 μm (%)	Calcite <10 μm (%)	Quartz (%)	Dolomite (%)	Selvage (%)	% Compaction volume loss by solution	% Tectonic volume loss by solution	Finite strain ellipse ratio for GBS[b]	Constant volume shortening (%)
13	Helderberg	G	75.7	19.5	4.8	0.0	0.0	11.5	7.5		
14	Tonoloway	M	1.2	95.3	0.0	0.0	3.1	10.3	2.8		
17	Helderberg	P	49.3	46.3	0.8	0.0	3.7	20.0	13.3		
18	Tonoloway	W/P	26.5	73.5	0.0	0.0	0.0	4.0	0.0	1.06[c]	2.9
35	Tonoloway	M	2.2	95.3	0.0	0.0	1.5	21.0	4.7		
36	Tonoloway	W	19.3	68.3	0.0	12.3	0.0	1.0	0.0	1.06[c]	2.9
37	Helderberg	P	92.3	4.2	0.0	0.0	1.5	4.5	2.0		
38	Tonoloway	M	3.3	95.3	0.0	0.0	1.3	12.8	3.0		
39	Tonoloway	M	0.0	96.7	0.0	3.3	0.0	4.0	0.0		
44	Tonoloway	W	19.2	80.0	0.8	0.0	0.0	0.0	0.0	1.09[c]	4.2
45	Tonoloway	W	17.6	81.0	0.0	0.8	0.0	5.0	3.0	1.20[c]	8.7
51	Tonoloway	M	1.4	84.7	0.7	0.3	12.9	11.2	3.5		
53	Helderberg	P	91.3	8.7	0.0	0.0	0.0	20.0	6.3		
54	Helderberg	P	80.1	16.9	3.0	0.0	0.0	6.0	0.0		
55	Helderberg	P	67.4	32.5	0.0	2.8	0.0	9.3	2.0		
56	Tonoloway	W	95.0	5.0	0.0	0.0	0.0	6.0	0.0		
58	Tonoloway	W	34.7	65.3	0.0	0.0	0.0	6.0	0.0		
65	Helderberg	P	37.7	61.3	1.0	0.0	0.0	8.0	7.7		
66	Tonoloway	W/P	32.7	64.0	0.3	3.0	0.0	6.0	3.0		
67	Tonoloway	W	30.7	66.3	0.0	1.3	1.7	19.5	3.3		
68	Helderberg	P	89.3	5.3	1.7	0.0	3.7	35.0	10.0		
69	Tonoloway	W	71.6	16.0	12.4	0.0	0.0	5.0	0.0		
70	Tonoloway	G	75.7	24.3	0.0	0.0	0.0	6.0	1.0		
72	Tonoloway	W	72.5	17.0	10.5	0.0	0.0	10.0	3.0		
74	Helderberg	M	1.3	67.7	5.7	25.0	0.3	8.8	1.8		
77	Tonoloway	W	66.3	20.3	10.3	0.0	3.0	4.0	2.0		
78	Tonoloway	W	7.3	91.7	0.0	0.0	1.0	13.4	5.3		
80	Tonoloway	W/P	23.7	75.3	1.0	0.0	0.0	3.2	5.4		
83	Tonoloway	M	1.8	95.3	0.0	1.8	1.0	9.1	3.4		
84	Tonoloway	M	1.4	98.6	0.0	0.0	0.0	5.6	0.0		
85	Tonoloway	G	43.8	56.2	0.0	0.0	0.0	0.0	0.0		
99	Helderberg	P	90.3	2.0	1.0	4.7	2.3	10.7	4.4		
109	Helderberg	P	89.7	4.0	4.7	1.7	0.0	4.5	3.4		
111	Tonoloway	W	15.0	81.3	0.3	0.3	0.0	0.0	0.0	1.69	26.0
112	Tonoloway	W	33.3	66.7	0.0	0.0	0.0	1.0	0.0	1.63	27.0

[a] G = grainstone, M = mudstone, P = packstone, W = wackestone.
[b] GBS in grain-boundary-sliding.
[c] In plane normal to bedding and parallel to dip.

Table 4
Calcite twin strain data

Site	e_1[a]	Plunge and trend (geographic)	e_2[a]	Plunge and trend (geographic)	e_3[a]	Plunge and trend (geographic)	%NEV[b]	Error
13	3.09	14/348	0.69	49/099	−3.78	34/244	25	0.51
14	1.11	14/190	0.78	56/079	−1.89	30/288	15	0.22
17	0.85	16/035	0.31	42/286	−1.16	40/140	34	0.25
18	0.68	64/308	0.01	20/174	−0.69	18/079	15	0.09
37	1.74	67/100	0.29	7/163	−2.03	23/295	20	0.39
53	2.77	57/222	0.44	28/023	−3.21	13/114	2	0.36
54	3.08	82/007	−0.91	8/244	−2.18	10/154	31	0.78
55	1.97	70/315	−0.63	4/058	−1.34	20/148	53	0.45
65	1.67	34/331	0.38	10/216	−2.05	48/112	16	0.30
68	2.70	25/076	0.68	22/176	−3.38	54/304	25	0.62
70	2.55	40/198	1.81	36/070	−4.35	30/315	18	0.60
77	6.08	40/308	−0.27	16/048	−5.91	47/158	10	0.87
80	0.40	29/085	0.06	68/351	−0.46	2/165	32	0.12
99	4.45	75/156	−0.20	9/047	−4.25	16/316	21	0.66
109	0.65	56/251	0.13	32/072	−0.78	0/340	22	0.13

[a] e_1 = maximum extension, e_2 = intermediate extension, and e_3 = minimum extension.
[b] %NEV = % negative expected values.

infer to be evidence for prefolding layer-parallel shortening. The lack of later, nonlayer-parallel twin strain is common in limestones deformed at low temperatures and is attributed to strain hardening (Spang and Groshong, 1981; Kilsdonk and Wiltschko, 1988; Evans and Dunne, 1991; Harris and van der Pluijm, 1998). After restoring bedding to horizontal, the average maximum shortening (minimum extension, e_3) direction is 313° (Fig. 12b), and the minimum and intermediate shortening (maximum (e_1), and intermediate (e_2) extensions, respectively) directions fall along a girdle (Fig. 12b). The fold axial trends for the Patterson Creek and Wills Mountain anticlines are 026° and 030°, respectively, so the shortening direction is within 13–17° of fold normal. The average shortening direction determined from twinning is close to that determined from tectonic stylolites (Fig. 12b). Twin strain shows no preference for apparent constriction or apparent flattening on a Flinn diagram (Fig. 13a).

6.3. Diffusion-accommodated grain-boundary sliding

Strain due to diffusion-accommodated grain-boundary sliding can only be determined in fine-grained rocks where passive markers exist such as pellet outlines. In this study, the normalized Fry method (Fry, 1979; Erslev, 1988) is used to determine this strain with micritized carbonate pellets or ooids as markers (Fig. 14). The grain-size for these markers is generally less than 10 μm, and if no other mechanisms were operative, the total strain may be attributed to grain boundary sliding.

Six sites (18, 36, 44, 45, 111, 112) with mudstone and wackestone contain the 100–200 pellets and/or ooids on at least one thin section necessary to determine strain by the normalized Fry method (Table 5). Only four sites (44, 45, 111, 112), however, yielded three mutually perpendicular sections with sufficient markers to determine a finite strain ellipsoid. For the remaining sites, only the vertical, dip-parallel section was used to estimate a *X*/*Z* strain ellipse. The measured strain in all samples is dominated by compaction (Table 5, Figs. 9 and 10). We recognize that strain attributed to grain-boundary sliding may be present in the remaining fine-grained samples, but it cannot be measured because of a lack of strain markers.

Table 5
Finite strain data

Site	e_1[a] (%)	Plunge and trend (geographic)	e_2[a] (%)	Plunge and trend (geographic)	e_3[a] (%)	Plunge and trend (geographic)	*X*/*Z* ratio[b]	Rake of *X*[c]
18							1.06	2°
36							1.06	3°
44	3.13	30/129	2.11	1/220	−5.04	60/312	1.09	1°
45	7.55	1/204	6.48	12/114	−12.68	78/295	1.20	17°
111	19.11	19/194	14.53	26/094	−26.70	57/316	1.58	9°
112	25.65	8/182	7.40	30/087	−25.90	58/286	1.48	5°

[a] e_1 = maximum extension, e_2 = intermediate extension, and e_3 = minimum extension.
[b] *X*/*Z* ratio is finite strain ellipse ratio on vertical plane parallel to bedding dip.
[c] Rake of long axis of strain ellipse in dip plane with respect to bedding surface.

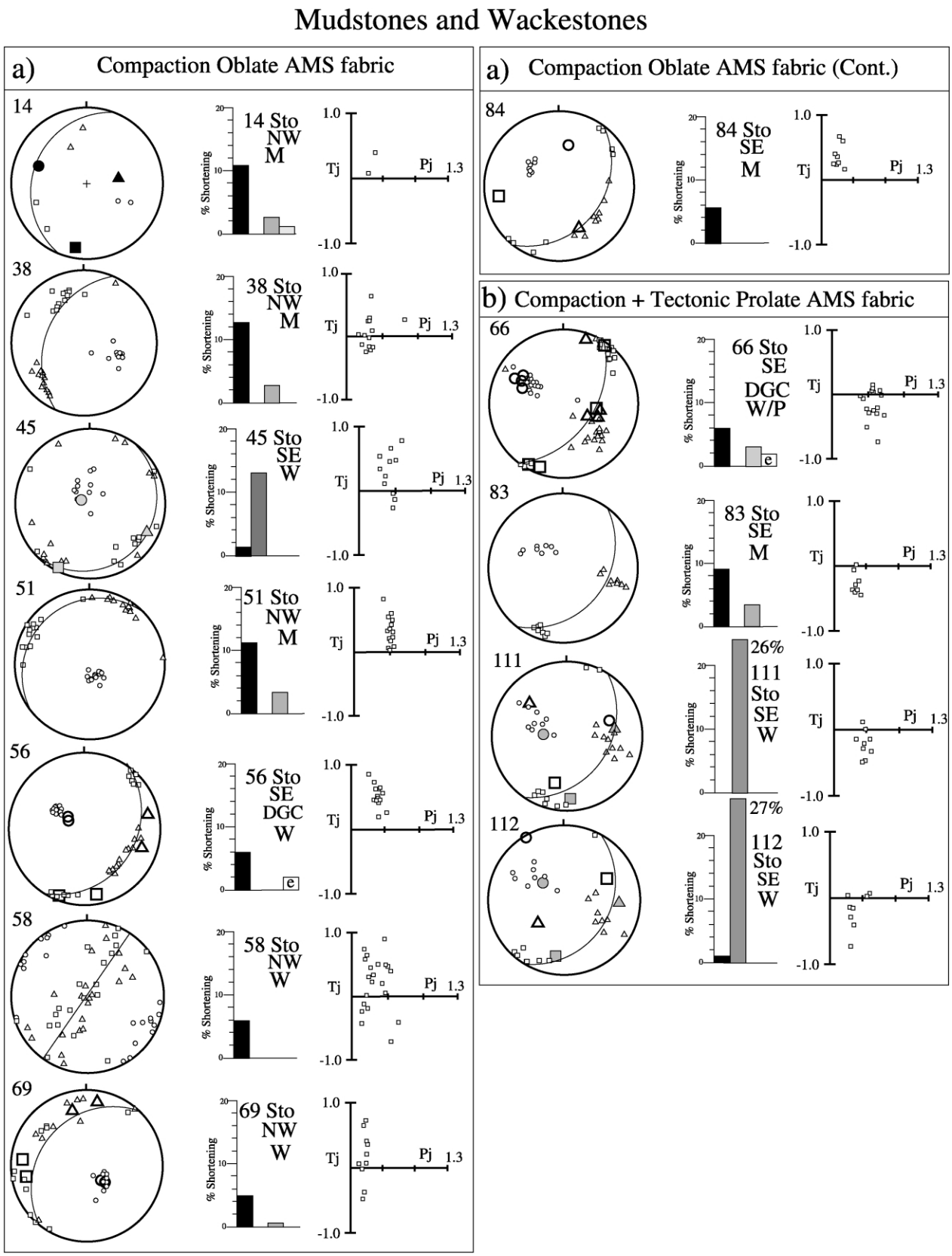

Fig. 9. Summary diagram showing AMS ellipsoid, strain partitioning and P_j/T_j plot for each sample site of mudstones (M) and wackstones (W) as grouped by AMS ellipsoid type (a)–(e). Equal area, lower hemisphere stereonets show AMS ellipsoid axes, AARM ellipsoid axes, twin strain ellipsoid axes, finite strain ellipsoid axes, bedding plane. Dhl is Helderberg Group and Sto is Tonoloway Formation. Bed dip is shown as either NW or SE. DCG indicates evidence for dislocation mechanisms. 'e' in sites 56, 66, 67, and 72 indicates that the twinning strain is estimated because of the presence of bent twins. Key for the histograms and stereonet symbols is shown on the bottom right.

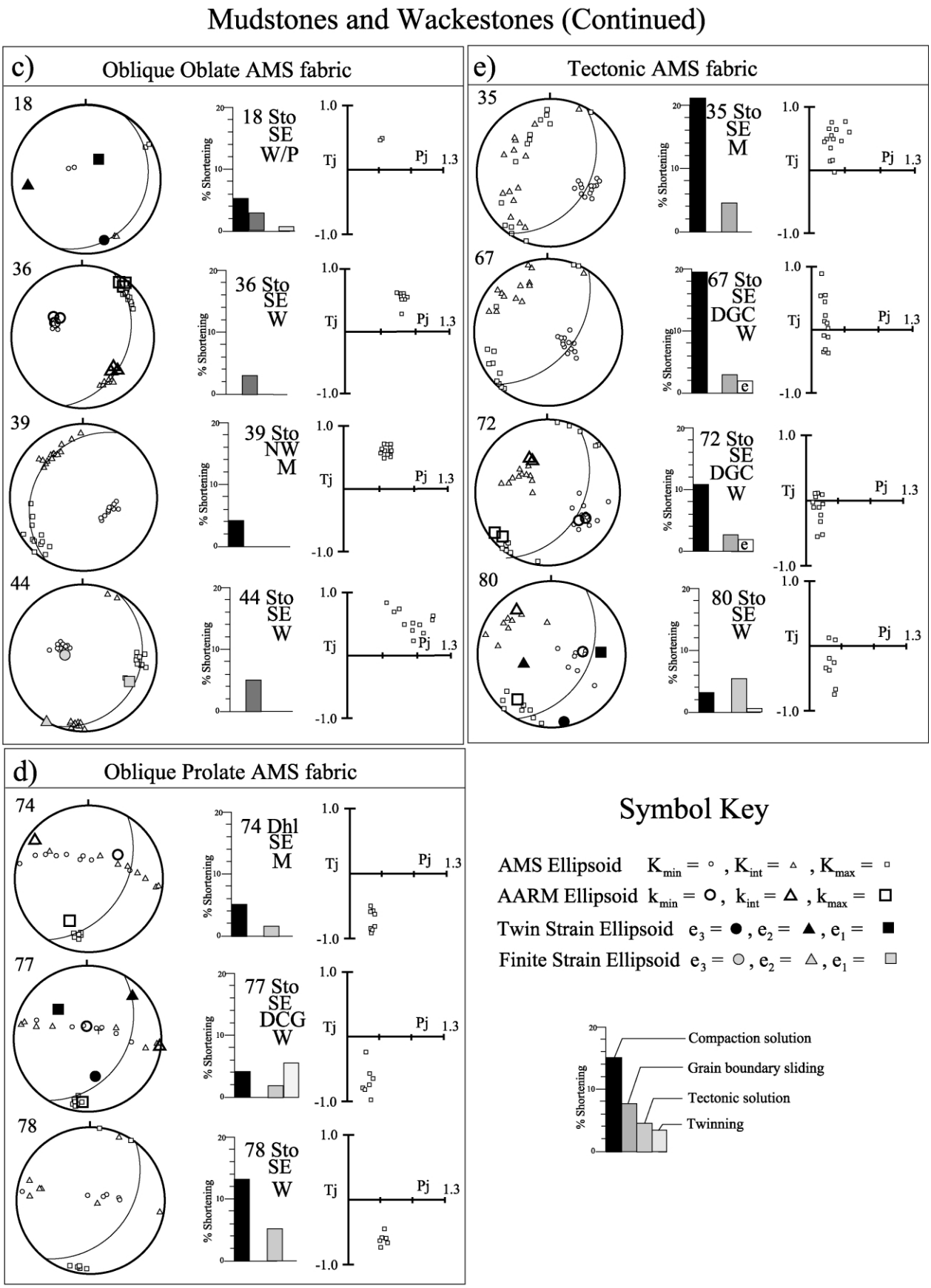

Fig. 9 (*continued*)

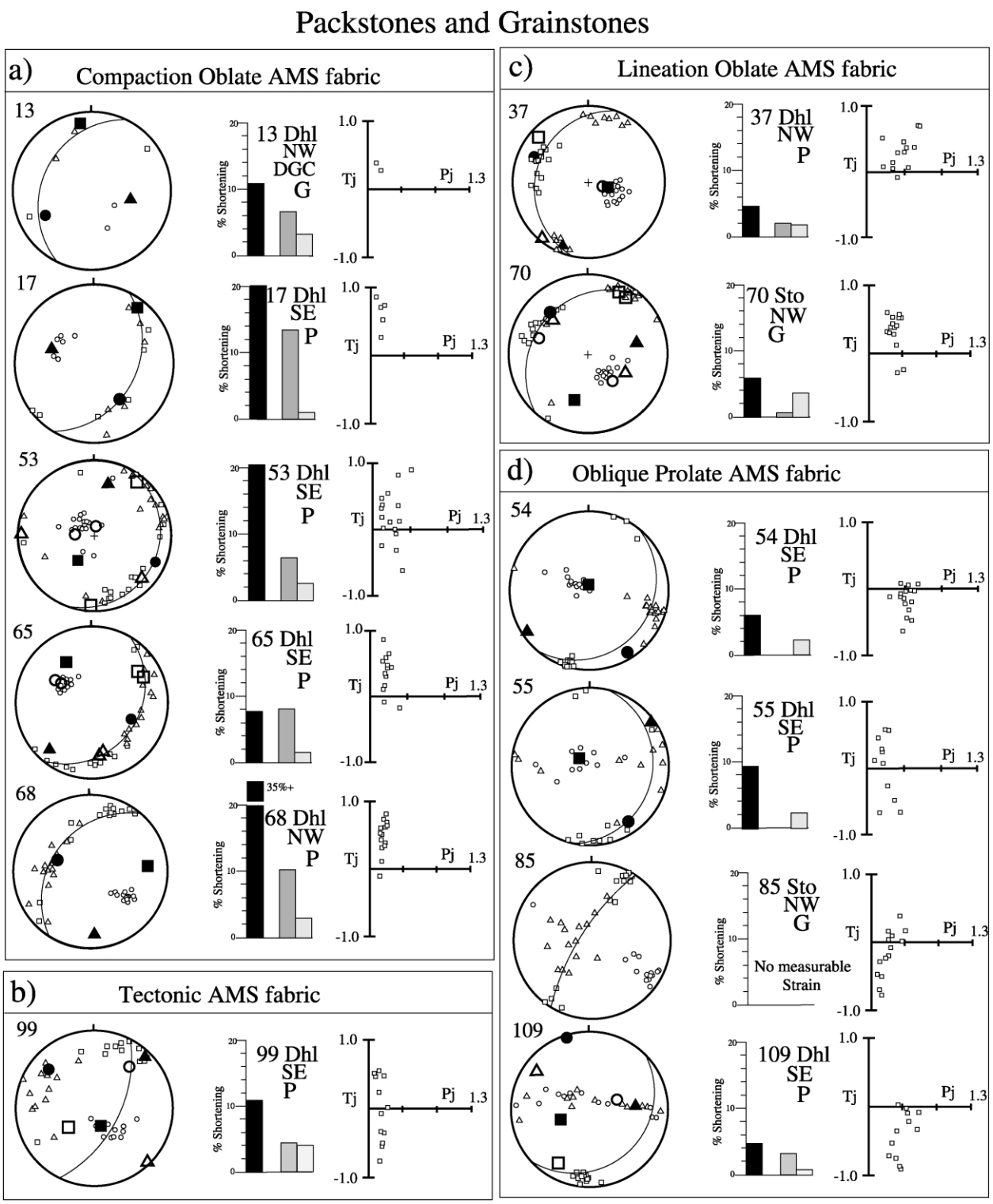

Fig. 10. Summary diagram showing AMS ellipsoid, strain partitioning and P_j/T_j plot for each sample site of packstones (P) and grainstones (G) as grouped by AMS ellipsoid type (a)–(d). Equal area, lower hemisphere stereonets show AMS ellipsoid axes, AARM ellipsoid axes, twin strain ellipsoid axes, finite strain ellipsoid axes, bedding plane. Dhl is Helderberg Group and Sto is Tonoloway Formation. Bed dip is shown as either NW or SE. DCG indicates evidence for dislocation mechanisms. Key for the histograms and stereonet symbols is shown in Fig. 9.

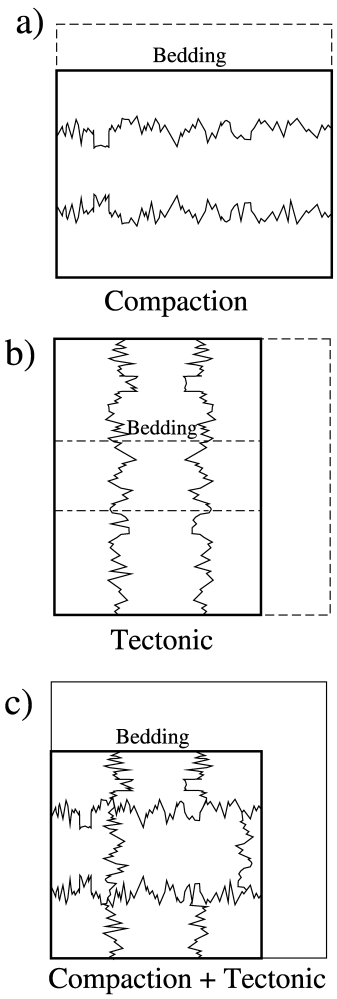

Fig. 11. Schematic diagram showing partitioning of pressure solution. (a) Compactional solution with bed-parallel stylolites, (b) pre-folding tectonic solution with bed-normal stylolites, and (c) rock containing both kinds of solution structures.

6.4. Dislocation glide and climb

The presence of dislocation-related distorted grains is inferred for six sites (13, 56, 66, 67, 72, 77) based on the presence of bent twins and undulose extinction. Strain magnitudes were not measured due to the difficulty in quantifying the contribution of dislocation mechanisms to the finite strain.

7. AMS and AARM results

7.1. AMS results

For the packstones and grainstones, the site mean bulk susceptibilities (K_m) range from 37 to 259×10^{-6} SI with an average value of 120×10^{-6} SI. For the mudstones and wackestones, the bulk mean susceptibilities are 48 to 537×10^{-6} SI with an average value of 210×10^{-6} SI (Fig. 15). The smaller values are typical of calcite and ferroan calcite (-13 to $\sim 200 \times 10^{-6}$ SI; Rochette, 1988; Tarling and Hrouda, 1993) while the larger values are indicative of the presence of high susceptibility minerals such as dolomite, siderite, chlorite, goethite, or ferromagnetic minerals such as magnetite (Rochette, 1988; Tarling and Hrouda, 1993). The sites with the greatest K_m values are rich in high susceptibility minerals (compare Tables 1 and 3). For example, site 51 ($K_m = 537 \times 10^{-6}$ SI) contains 12.9% stylolite selvage material that is rich in chlorite and magnetite, and site 36 ($K_m = 484 \times 10^{-6}$ SI) contains 12.3% ferroan dolomite. Sites 38 ($K_m = 408 \times 10^{-6}$ SI) and site 78 ($K_m = 584 \times 10^{-6}$ SI), however, do not have any obvious high susceptibility minerals. There is apparent correlation between the presence of the high susceptibility minerals and an increase in degree of anisotropy (P_j) in these samples (Fig. 15).

Six basic AMS ellipsoid shape-bedding relationships are defined in this study on the basis of the K_{min}, K_{int}, and K_{max} geometry relative to bedding (Fig. 16, Table 6). It should be noted that due to scatter in the data (Figs. 9 and 10) there is actually a continuum between the end-member ellipsoid types. However, the AMS ellipsoids fall into relatively discrete fields on the AMS Flinn diagrams (Fig. 17) and supports the interpreted similarity within groupings. Except for those samples

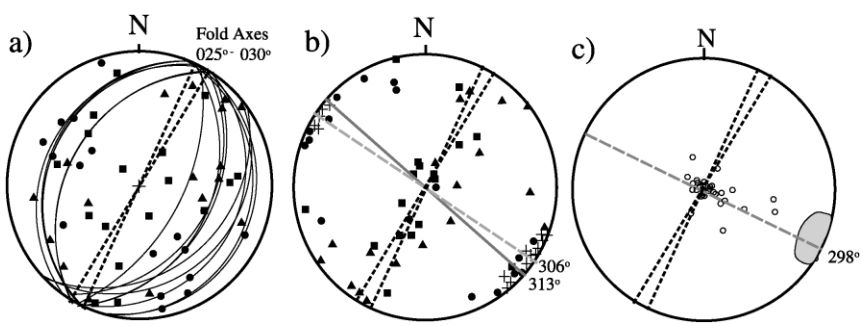

Fig. 12. Equal area, lower hemisphere stereonets showing (a) calcite twinning strain ellipsoid axes in geographic coordinates and (b) with bedding dip removed at all stations. Also included are poles to tectonic stylolites (crosses), average shortening directions for calcite twinning strain (solid line) and tectonic stylolites (dashed line), and average fold axes (dotted lines). (c) K_{min} orientations for all samples. Dashed line circles are those interpreted as having a tectonic fabric. Curved lines in (a) are bedding traces. In (a) and (b), solid circles are e_3, solid triangles are e_2, and solid squares are e_1.

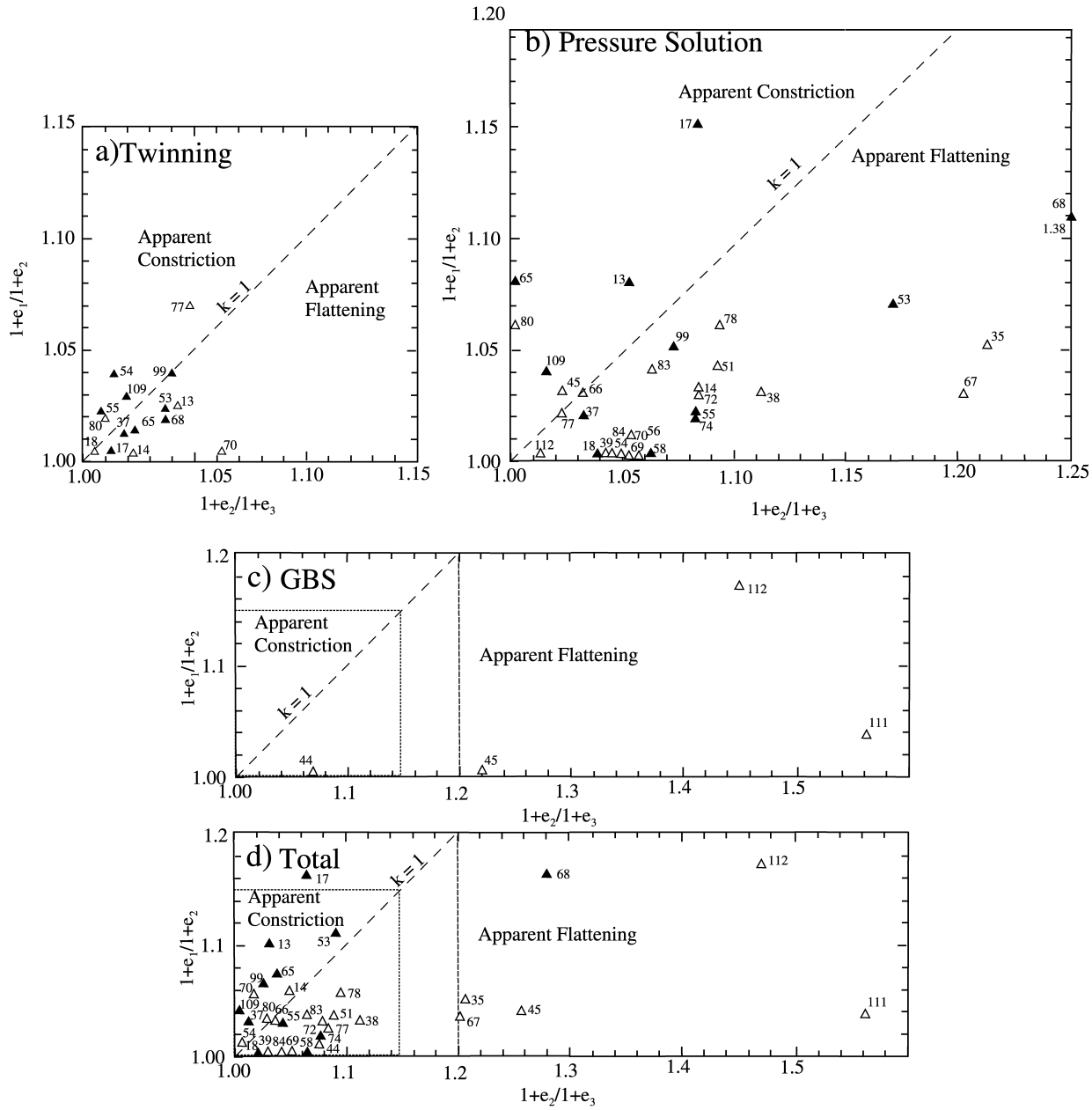

Fig. 13. Flinn diagrams for (a) strain due to twinning (b) solution strain, (c) grain-boundary sliding, and (d) total strain. Helderberg Group are solid triangles, Tonoloway Formation are open triangles.

with a Tectonic AMS shape (Fig. 16d), nearly all samples have K_{min} normal to bedding (Fig. 12c) indicating that compaction dominates the AMS fabric. Mudstone and wackestone AMS ellipsoids fall into discrete fields on a Flinn diagram (Fig. 17a) while packstone and grainstone sites show less well defined clusters (Fig. 17b).

7.2. AARM results

AARM ellipsoid anisotropies are high, ranging from 4.5 to >23%, indicating a strong preferential orientation of magnetite grains in the rocks. AARM ellipsoid shape (Fig. 18, Table 4) shows no relationship with either AMS ellipsoid shape (Fig. 17) or strain ellipsoid shape (Fig. 13). However, in 13 of 17 sites, the AMS and AARM ellipsoid axes are nearly coincident (Figs. 9 and 10), indicating that the same factors controlling the shape of the AMS ellipsoid also influences the AARM ellipsoid. In particular, the short axes of the ellipsoids are commonly bed normal, indicating a strong compaction component. In the remaining five samples (sites 84, 99, 111, 112), the correlation between AMS and AARM ellipsoid axes is poor.

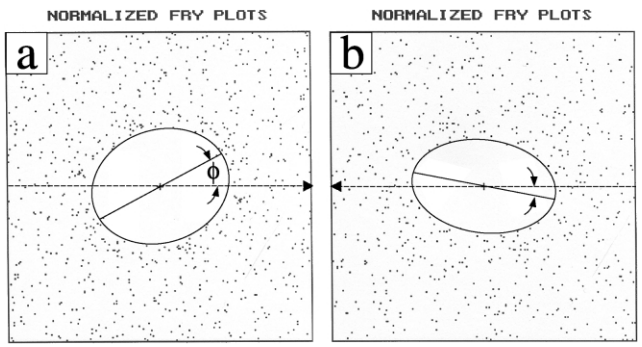

Fig. 14. Examples of normalized Fry diagrams in vertical sections that are parallel to bedding dip. (a) site 45 and (b) site 112. Dashed line is trace of bedding and arrow is dip direction. Dark line is long axis (X) of ellipse, and f is angle between long axis and bedding trace.

8. Integrating AMS, AARM, and strain data

8.1. Mudstones and wackestones

8.1.1. Compactional oblate fabrics

Sites 14, 38, 45, 51, 56, 58, 69, and 84 all exhibit moderately oblate compactional fabrics with the K_{int} and K_{max} girdle in the bedding plane (Tables 1 and 6, Figs. 9 and 17a). All samples exhibit compactional partial strain due to pressure solution (Table 3, Fig. 9a). Also, the samples (14, 38, 51) with a tectonic partial strain due to pressure solution show tighter clusters of K_{int} and K_{max} in the AMS girdles. Except for site 84, AARM and AMS ellipsoid axes are nearly coincident, indicating that the magnetite is aligned in the plane of bedding and may be contributing to the AMS. Therefore, these fabrics are interpreted to result from phyllosilicate and magnetite alignment along solution structures, with the greater alignment parallel to bedding because of compactional solution is greater than tectonic. The random orientation of phyllosilicate crystal K_{max} and K_{int} axes in solution structures causes samples with large amounts of compactional solution strain to have a wide dispersion of T_j (shape factor) values (Fig. 9).

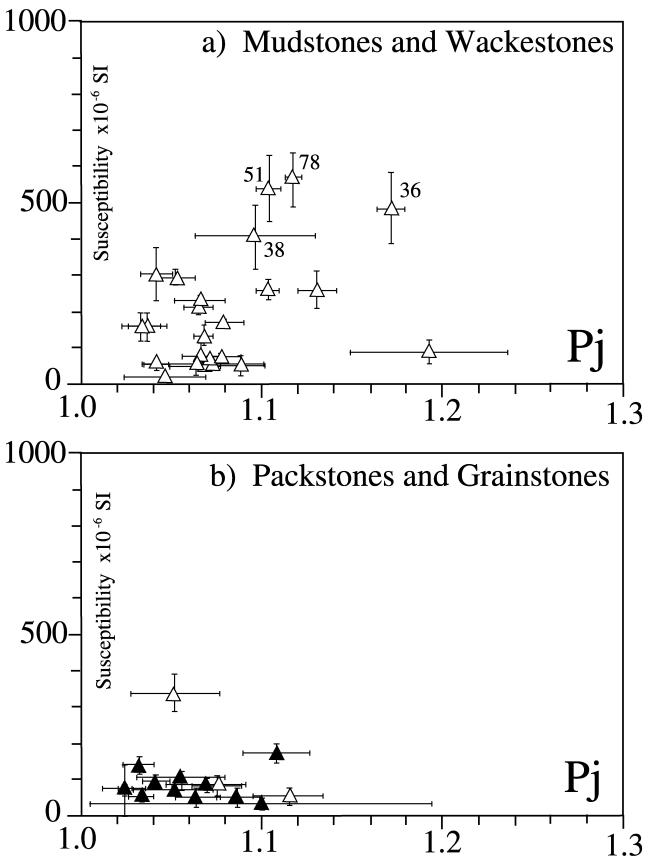

Fig. 15. Plots of K_m versus P_j for (a) mudstone and wackestones and (b) packstones and grainstones. Lines show one standard deviation in values. Symbols are the same as in Fig. 13.

8.1.2. Compaction–tectonic prolate fabric

Sites 66, 83, 111, and 112 all have K_{int} parallel to bedding dip, K_{min} normal to bedding, and K_{max} parallel to strike (Tables 1 and 6, Fig. 9b). The AMS ellipsoid shape is moderately prolate (Fig. 17a). Sites 66 and 83 have nearly the same ratio of compaction/tectonic solution and an AMS fabric that is interpreted as a composite fabric resulting from aligned phyllosilicates and magnetite in both compaction and tectonic solution structures. The strong agreement between AARM and AMS ellipsoid axes in site 66 shows that magnetite grains are aligned, presumably in the solution structures.

Sites 111 and 112 both show a large component of compaction (up to 27% shortening) manifested as flattened ooids and pellets. There is little evidence for pressure solution either at the grain-to-grain scale or as stylolites. Therefore, the strain is interpreted to be due to grain-boundary-sliding. The calculated finite strain ellipsoid matches the AMS ellipsoid orientation, indicating that rotation and/or recrystallization of disseminated phyllosilicates may control the AMS. In both samples, the orientation of the K_{int} axis and the intermediate shortening axis in the down-dip direction indicate a slight tectonic component overprinting the compaction. Although sites 111 and 112 exhibit high compactional strain, there is little agreement between the AARM and AMS axes. This may reflect the lack of magnetite reorientation by grain-boundary sliding.

8.1.3. Oblique oblate fabrics

Oblique oblate fabrics are defined by AMS ellipsoid K_{min} axes that are normal to bedding, and K_{int} and K_{max} axes that are in the bedding plane yet oblique to the dip direction. Sites 18, 36, 39, and 44 have this strongly oblate fabric (Tables 1 and 6, Figs. 9c and 17a). Nearly all recorded partial strains are due to minor solution and grain-boundary sliding, and are compactional, which is consistent with K_{min} normal to bedding. K_{int} is moderately well clustered in the bedding plane and indicates a tectonic layer parallel shortening. This is supported by calcite twin strain determined for site 18 where the e_3 axis is parallel to the K_{min} direction.

Interestingly, these four sites exhibit the smallest total

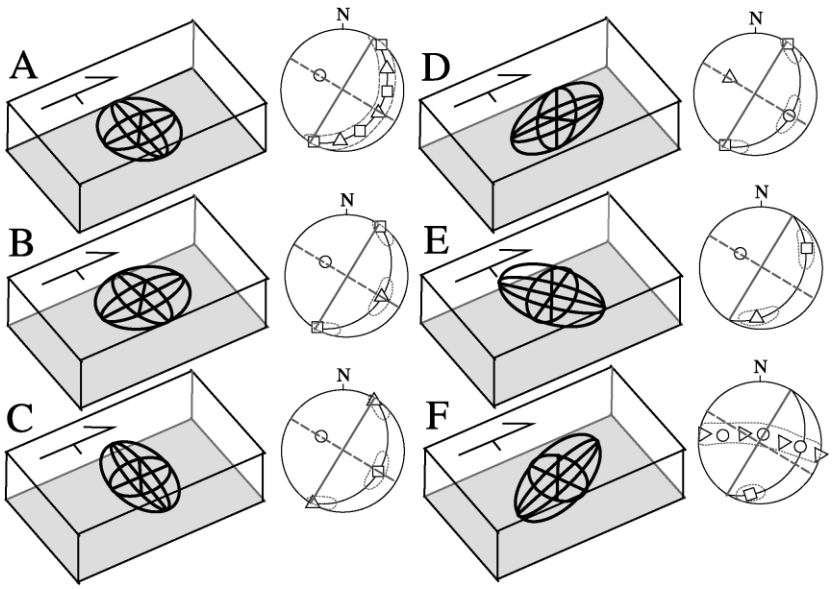

Fig. 16. Types of susceptibility ellipsoids (Table 6) shown in relation to bedding. Stereonets show AMS ellipsoid axes. Open circles are K_{min}, open triangles are K_{int}, and open squares are K_{max}. Dashed outlines indicate range of axis distribution. Straight line across stereonet is strike and dashed line is parallel to dip direction. On blocks, lines with arrows are bedding orientation symbols with arrow pointing in strike direction, and short line in dip direction.

strains of all samples examined, yet they have the largest degree of anisotropy (P_j) values. One possibility is that these samples all contain a strong depositional fabric involving micrite-size grains and disseminated phyllosilicates. Therefore, in sites 36 and 44, we interpret the AMS fabric to be due to aligned disseminated phyllosilicate minerals because these samples lack a grain-shape fabric and solution structures that would align other possible magnetic minerals. However, AARM data for site 36 shows a strong agreement with the AMS fabric, indicating that SD magnetite grains are also aligned. In sites 18 and 39, aligned phyllosilicates and magnetite in solution structures may also contribute to the AMS fabric.

8.1.4. Oblique prolate fabric

Sites 74, 77, and 78 have a strongly prolate AMS fabric (Fig. 17a) with the K_{min} and K_{int} girdle normal to bedding and K_{max} in the bedding plane, but oriented oblique to bedding strike (Tables 1 and 6, Fig. 9d). These samples all have a tectonic partial strain due to solution that is approximately equal to one-half that of the compaction partial strain. Since AARM and AMS data agree in sites 74 and 77, aligned phyllosilicates and magnetite within the compaction and tectonic solution zones are interpreted to contribute bed parallel and bed normal oblate AMS components, respectively. The addition of these fabrics result in a prolate composite fabric with the K_{max} axis parallel to strike.

8.1.5. Tectonic fabric

Sites 35, 67, 72 and 80 have a weakly oblate to weakly prolate tectonic AMS fabric (Fig. 17a) with K_{min} parallel to bedding dip (Table 1, Fig. 9e). Although a moderate tectonic solution strain is measured, cleavage is not recognizable in either outcrop or thin section. Sites 35, 67, and 72 are from the steep limbs of mesoscale folds, and may have experienced localized high strain associated with folding. However, except in site 80, compaction partial strain is

Table 6
AMS ellipsoid types

Type	Shape	K_{min}-bedding relationship	K_{max}-bedding relationship	Sites
Compaction oblate	Weak triaxial oblate to uniaxial oblate	Normal to bedding	Scattered in bedding plane	13?, 14, 17, 38, 51, 53, 56, 58, 65, 68, 69, 84
Compaction + tectonic prolate	Triaxial prolate	Normal to bedding	Parallel to strike	55, 66, 83, 85, 111, 112
Lineation oblate	Triaxial oblate	Normal to bedding	Parallel to dip	37, 70
Tectonic	Triaxial oblate to triaxial prolate	Parallel to dip	Normal to bedding	35, 67, 72, 80, 99
Oblique prolate	Triaxail prolate to uniaxial prolate	Scattered in plane normal to bedding	In bedding plane, toward SE quadrant	54, 74, 77, 78, 109
Oblique oblate	Triaxial oblate	Normal to bedding	In bedding plane, toward NE quadrant	18, 36, 39,44

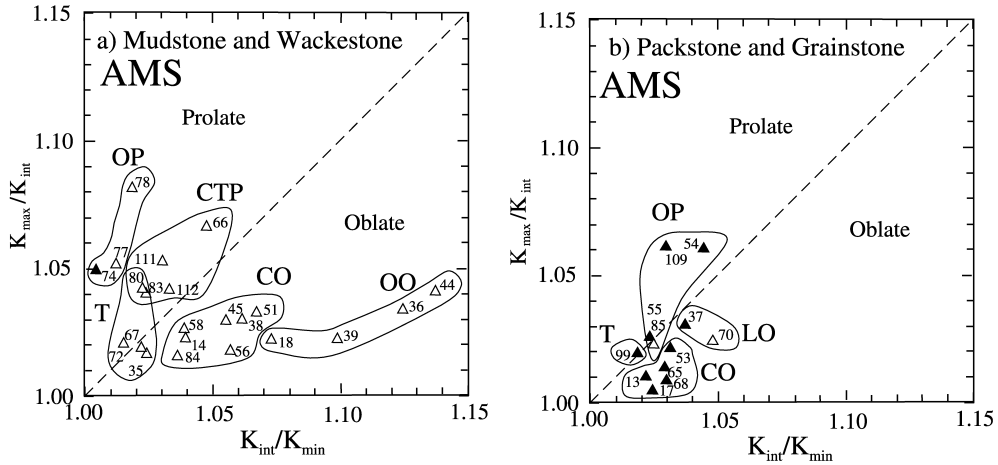

Fig. 17. Flinn diagrams for AMS ellipsoid shapes of (a) mudstones and wackstones, and (b) packstones and grainstones. Symbols are the same as in Fig. 12. Outlined groups show ellipsoid shapes as interpreted in the text and Table 5: CO = Compaction oblate, CTP = Compaction–tectonic prolate, LO = Lineation oblate, OO = Oblique oblate, OP = Oblique prolate, and T = Tectonic.

much greater than tectonic partial strain and a compaction oblate fabric would be expected. One possibility is that enough new magnetite grains grew in the tectonic solution structures during deformation so as to override the compaction signal and control the AMS response, or significantly more magnetite is aligned along tectonic stylolites than compaction stylolites. Both possibilities are supported by the agreement between AARM and AMS ellipsoid axes in sites 72 and 80. Alternatively, phyllosilicate and magnetite alignment along common, but unmeasurable, grain-to-grain solution zones may be making a significant contribution to the Tectonic AMS fabric. In the coarser-grained rocks common bent calcite twins provide evidence for grain distortion by dislocation mechanisms. Ferroan calcite grains distorted by twinning and dislocation

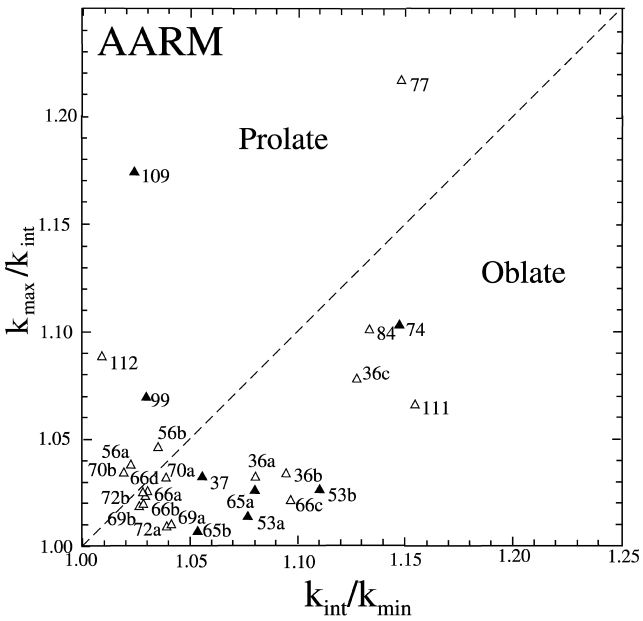

Fig. 18. Flinn diagram of AARM ellipsoid shapes. Symbols are the same as in Fig. 13.

mechanisms may also contribute to the tectonic AMS component in sites 67 and 72.

8.2. Packstones and grainstones

8.2.1. Compaction oblate fabric

Sites 13, 17, 53, 65, and 68 exhibit a moderately oblate compaction fabric (Tables 1 and 6, Figs. 10a and 17b). In sites 53 and 65, AARM and AMS ellipsoid minimum axes are coincident, and AARM intermediate and maximum axes lie in the bedding plane reflecting an alignment of magnetite grains in the solution structures. The AMS fabric is therefore interpreted to be a composite fabric, primarily due to aligned phyllosilicates and magnetite along compaction solution structures (up to 35% partial strain) and tectonic solution structures (up to 13% partial strain). Unlike the finer grained rocks, the intermediate axes do not tend to cluster with increasing tectonic solution. This may be due to an overprinting of an inverse AMS fabric from the relatively high calcite twinning (up to nearly 4%), which would counteract the response from phyllosilicate alignment along the tectonic solution zones.

8.2.2. Tectonic fabric

Site 99 is from an overturned bed on the northwest limb of the Wills Mt. anticline and is the only coarse-grained rock with a tectonic fabric (Tables 1 and 6, Figs. 10b and 17b). The minimum extension axis due to twinning is subhorizontal in geographic coordinates and indicates post-folding flattening. As with the tectonic fabric in the fine-grained rocks, aligned phyllosilicates and magnetite along solution structures are interpreted to control the AMS fabric. However, an inverse contribution by twinning may be important since the maximum extension axis is coincident with the K_{min} axis of the AMS ellipsoid. In site 99, the AARM and AMS ellipsoid orientations are different, indicating little contribution by magnetite to the AMS.

8.2.3. Lineation oblate fabric

Sites 37 and 70 have a triaxial oblate fabric (Fig. 17b) with K_{min} normal to bedding and K_{max} in the bedding plane and parallel to dip (Tables 1 and 6, Fig. 10c). Because the long axis of the AMS ellipsoid is parallel to dip, we have termed it a 'lineation' fabric. This apparently inverse fabric is interpreted to be a composite fabric resulting from twinning, which accounts for a large percentage of the total deformation, and aligned phyllosilicates in solution structures. The AARM and AMS ellipsoid axis orientations are coincident in site 37, but in site 70 they are reversed. This may be related to the presence of tectonically aligned magnetite in site 70 solution structures.

8.2.4. Oblique prolate fabric

Sites 54, 55, 85, and 109 have a moderately prolate fabric (Fig. 17b) with K_{int} and K_{max} oblique to bedding dip (Tables 1 and 6, Fig. 10d). These samples all have a small compaction partial strain due to solution ($<9\%$), and 1–2% shortening due to twinning. Only site 109 has a tectonic partial strain due to solution. Aligned phyllosilicates and magnetite within the solution structures are interpreted to control the AMS. However, the small twin strain may contribute an inverse component as shown by the coincidence of the minimum extensions axes and K_{max} in sites 55 and 109. Site 85, a biosparite, is anomalous in that it exhibits no strain at the thin section scale, yet has a well developed AMS fabric. This may be due to the strong primary depositional bed-parallel alignment of shell fragments. However, since the K_{int} axis is parallel to bedding dip, a component of tectonic layer-parallel shortening is also necessary, but is unrecognizable in the rock fabric.

9. Discussion

9.1. Strain heterogeneity

One of the most striking results of this study is the heterogeneity of the partitioned strain in terms of both deformation mechanism and strain magnitude. Close examination of Figs. 9 and 10 shows that each of the 35 samples examined in this study has a different distribution of partitioned strain. The total strain is the result of compaction manifested as solution structures and grain-boundary sliding; and layer-parallel-shortening manifested as twinning strain, solution structures, and grain-boundary sliding. Syn- to post-folding strain is minor since all the strain axes are either normal or parallel to bedding. Also, we do not see evidence for passive rotation of cleavage or other rock fabrics on the scale of the macrofolds (Meyer and Dunne, 1990; Stamatakos and Kodoma, 1991a,b).

We interpret the wide variety of partitioned strain histograms (Figs. 9 and 10) to be the function of two factors. First, rock lithology, which includes mineralogy, grain size, and clay content, controls the active deformation mechanisms. Although we sampled only limestones, the grain-size distribution of the rocks vary from mudstones to grainstones. The finer-grained rocks deformed primarily by grain-boundary sliding, while the coarser-grain rocks deformed primarily by twinning. Solution deformation is common in all rock types and the magnitude may reflect the clay content.

Second, bedding character will control how rocks respond to tectonic stress. Except for those sites associated with mesoscale folds (35, 67, 72, 99), all the sites sampled are from the relatively monotonously dipping limbs of the macroscale folds (Fig. 1). Therefore, the structural position within the macrofold is not likely to be a significant controlling factor in strain magnitude. Instead, bedding thickness may play a significant role in strain accumulation. The mudstones and the wackestones of the Tonoloway Formation are generally very thin-bedded (centimeters to decimeters), while the coarser-grained rocks of the Helderberg Formation have larger bedding thicknesses (decimeters to meters). The thin-bedded nature of the Tonoloway allows for tectonic strain to be accommodated by interbed slip manifested as disharmonic folding, while the thicker mechanical units of the Helderberg must deform internally. This is reflected in the higher tectonic strains in the thicker-bedded, coarser-grained rocks.

9.2. Strain and the AMS ellipsoid

The AMS ellipsoid shape is a product of a complex relationship between rock lithology, type of deformation mechanism, and magnitude of partitioned strain. In the limestones examined in this study, all of these factors are extremely variable at the scale of the sampled mesoscale folds. Such heterogeneity precludes the development of a simple quantitative relationship between AMS and finite strain. This is shown by the strikingly different distribution of sites in the AMS Flinn diagrams (Fig. 17) compared with the total strain Flinn diagram (Fig. 13d). Even when the strain is partitioned into deformation mechanisms, the relationship between AMS and partitioned strain is not simple (compare Figs. 13a–c and 17).

However, by examining similarities in partitioned strain within each of the six AMS ellipsoid shape-bedding relationships defined in Fig. 16 and Table 6, we can make

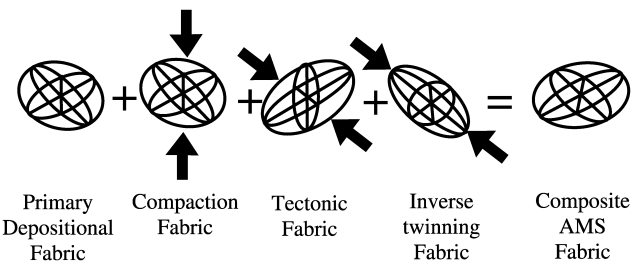

Fig. 19. Diagram illustrating the AMS fabrics comprising the final composite AMS ellipsoid.

several important qualitative observations on the AMS–strain relationship in the Helderberg and Tonoloway limestones.

Each of the AMS fabrics observed in the rocks is a composite, or a summation, of the primary AMS fabric, a compaction fabric, and a tectonic fabric (Fig. 19). First, all sedimentary rocks have an inherent primary depositional AMS fabric that is attributed to preferentially oriented phyllosilicates and is commonly bed-parallel uniaxial oblate (Tarling and Hrouda, 1993). However, the primary fabric is difficult to determine except in the rare instances where the rocks are demonstrably unstrained. All of the sites in this study exhibit some degree of compaction and/or tectonic strain, so we are not able to isolate the depositional fabric.

Second, a diagenetic and/or compaction bed-parallel uniaxial oblate AMS fabric formed during burial (Fig. 19). In this study, 27 of 35 sites have the K_{min} axis nearly normal to bedding, and all 35 have the K_{max} axis within the bedding plane, indicating that compaction dominates the AMS fabric. We assume that aligned primary and/or diagenetic phyllosilicates in the rock matrix are the primary contributor to this fabric. Whether the alignment is due to passive grain rotation or syn-compactional grain growth has not been determined. Where compaction solution structures are present, concentrated, realigned, and newly-formed paramagnetic phyllosilicates enhance the compaction fabric.

The presence and amount of magnetite within the solution structures will also affect the resulting AMS fabric. The strong correlation in some samples (e.g. 56, 69, 80) between AARM and AMS, SEM studies of stylolite zones, and the paleomagnetic work of Lewchuk et al. (2003)) demonstrate that new or realigned magnetite may be an important constituent of solution structures.

While solution strain contributes significantly to total strain, it does not proportionally affect the AMS ellipsoid shape (compare Figs. 13b and 17) or the AARM ellipsoid shape (compare Figs. 13b and 17). This is probably the result of variable amounts of phyllosilicates and the presence or absence of aligned magnetite within the solution structures.

Third, a tectonic bed-normal and strike-parallel biaxial oblate AMS fabric (Fig. 19) was imparted on the rocks by layer-parallel-shortening deformation prior to folding. This shortening is manifested by bed-normal tectonic stylolites that contain aligned phyllosilicates and magnetite. In addition, the orientation of K_{int} in the bedding dip direction in many samples without tectonic solution structures (e.g. sites 36, 39, 56, 84, 85, 111, 112) indicates that there is also an alignment of matrix phyllosilicates due to layer-parallel-shortening. As the tectonic strain increases, it initially overprints, then overrides the compactional AMS component, driving the AMS ellipsoid shape toward the prolate field.

Layer-parallel tectonic shortening is also reflected in calcite twinning strain, particularly in the coarse-grained packstones and grainstones. The inverse AMS fabric due to twinning is bed-parallel biaxial oblate with the long axis in the dip direction (Fig. 18). Where solution strain is low, and twinning strain is high, the inverse component may dominate the AMS fabric as interpreted for sites 37, 70, and 99. The similarity of site distributions in the oblate and prolate fields of the twin strain (Fig. 13a) and the AMS (Fig. 17) Flinn diagrams shows that the twin strain ellipsoid shape is a good predictor of the general AMS ellipsoid shape. We interpret this to mean that when twinning is a common deformation mechanism, it controls the AMS ellipsoid shape by grain distortion and reorientation of the K_{max} direction even when other mechanisms are present.

Finally, syn- to post-folding deformation does not appear to significantly affect either the accumulation of strain or the AMS response. Therefore, all strain and AMS fabrics are interpreted to be predominantly pre-folding in origin.

Importantly, since all AMS ellipsoids are actually composites of the AMS response from each deformation mechanism, similar AMS ellipsoid shapes and magnitudes may result from markedly different mechanisms and partitioned strains. For example, compare sites 111 and 112, which are wackestones dominated by grain-boundary-sliding strain, to sites 54, 66, and 83, which are a packstone, wackestone, and mudstone, respectively, and dominated by solution strain.

10. Conclusions

Strain partitioning in limestones is useful in evaluating the contribution of calcite deformation mechanisms to the anisotropy of magnetic susceptibility (AMS). The results of this study show that in a section of limestones where there is a variety of different lithologies based on mineralogy, grain size and clay content, each lithology responds differently to a particular set of deformation conditions. Therefore, although all the rocks have experienced the same deformation events, they will have markedly different partitioned strain distributions and AMS fabrics. In contrast, similar AMS ellipsoid shapes and magnitudes may result from different mechanisms and partitioned strains.

In the Helderberg and Tonoloway limestones, all AMS fabrics are composite fabrics resulting from the overprinting of three components: (1) an inherent primary depositional AMS fabric that is attributed to preferentially oriented phyllosilicates in the rock matrix; (2) a diagenetic and/or compaction AMS fabric formed during burial that is due to preferentially oriented phyllosilicates in solution structures and in the rock matrix; and (3) a tectonic AMS fabric that was imparted on the rocks by layer-parallel-shortening deformation prior to folding, and is also attributed to preferentially oriented phyllosilicates in solution structures and in the rock matrix, as well as twinning of ferroan calcite.

Acknowledgements

We acknowledge the support for this project from National Science Foundation grant EAR-9814913 to Evans and Elmore. We also thank J. Blachere and A. Stewart for assisting in the SEM work. Discussions with K. Kodama and W. Dunne were helpful in clarifying various aspects of the paper. We thank W. Dunne and an anonymous reviewer for providing valuable input into the final version of the manuscript. Ken Kodama and Eric Cox supplied the AARM data for this work.

References

Bathurst, R.G.C., 1971. Carbonate Sediments and Their Diagenesis, Elsevier, New York.

Bodou, P., 1976. L'importance des joints styolithiques dans la compaction des carbonates. Bull. Centre Rech. Pau SNPA 10, 627–644.

Borradaile, G.J., 1981. Particulate flow of rock and the formation of rock cleavage. Tectonophysics 24, 442–455.

Borradaile, G.J., 1987. Anisotropy of magnetic susceptibility: rock composition versus strain. Tectonophysics 138, 327–329.

Borradaile, G.J., 1988. Magnetic susceptibility, petrofabrics and strain. Tectonophysics 10, 1–20.

Borradaile, G.J., 1991. Correlation of strain with anisotropy of magnetic susceptibility (AMS). Pure and Applied Geophysics 135, 15–29.

Borradaile, G.J., Henry, B., 1997. Tectonic applications of magnetic susceptibility and its anisotropy. Earth Science Reviews 42, 49–93.

Borradaile, G.J., Mothersill, J.S., 1984. Coaxial deformed and magnetic fabrics without simply correlated magnitudes of principle values. Physics of Earth and Planetary Interiors 35, 294–300.

Borradaile, G.J., Sarvas, P., 1990. Magnetic susceptibility fabrics in slates, structural, mineralogical, and lithological influences. Tectonophysics 172, 215–222.

Borradaile, G.J., Tarling, D.H., 1981. The influence of deformation mechanisms on magnetic fabrics in weakly deformed rocks. Tectonophysics 77, 151–168.

Borradaile, G.J., Tarling, D.H., 1984. Strain partitioning and magnetic fabrics in particulate flow. Canadian Journal of Earth Sciences 21, 694–697.

Borradaile, G.J., Werner, T., 1994. Magnetic anisotropy and some phyllosilicates. Tectonophysics 235, 223–248.

Burkhard, M., 1990. Ductile deformation mechanisms in micritic limestones naturally deformed at low temperatures (150–350). In: Knipe, R.J., Rutter, E.H. (Eds.), Deformation Mechanisms, Rheology and Tectonics. Geological Society of London Special Publication 54, pp. 241–257.

Burkhard, M., 1993. Calcite twins, their geometry, appearance and significance as stress-strain markers and indicators of tectonic regime: a review. Journal of Structural Geology 15, 351–368.

Butler, R.F., Banerjee, S.K., 1975. Theoretical single-domain grain size range in magnetite and titanomagnetite. Journal of Geophysical Research 80, 4049–4058.

Cogne, J.P., Perroud, H., 1987. Unstraining paleomagnetic vectors: the current state of Debate. EOS, Transactions of the American Geophysical Union 67, 705–712.

Couzens, B.A., Dunne, W.M., Onasch, C.M., Glass, R., 1993. Strain variations and three dimensional strain factorization at the transition from the southern to central Appalachians. Journal of Structural Geology 15, 451–464.

Craddock, J.P., van der Pluijm, B.A., 1989. Late Paleozoic deformation of the cratonic carbonate cover of eastern North America. Geology 17, 416–419.

Dickson, J.A.D., 1966. Carbonate identification and genesis as revealed by staining. Journal of Sedimentary Petrology 36, 491–505.

Dorobek, S., 1987. Petrography, geochemistry, and origin of Burial diagenetic facies, Silurio-Devonian Helderberg Group (carbonate rocks), central Appalachians. American Association of Petroleum Geologists Bulletin 71, 492–514.

Dorobek, S., Read, J.F., 1986. Sedimentology and basin evolution of the Siluro-Devonian Helderberg Group, central Appalachians. Journal of Sedimentary Petrology 56, 601–613.

Dunne, W.M., 1996. The role of macroscale thrusts in the deformation of the Alleghenian roof sequence in the central Appalachians: a re-evaluation. American Journal of Science 296, 549–575.

Erslev, E.A., 1988. Normalized center-to-center strain analysis of packed aggregates. Journal of Structural Geology 10, 201–209.

Evans, M.A., Battles, D.A., 1999. Fluid inclusion and stable isotope analysis of veins from the central Appalachian Valley and Ridge province: implications for regional synorogenic hydrologic structure and fluid migration. Geological Society of America Bulletin 111, 1841–1860.

Evans, M.A., Dunne, W.M., 1991. Strain factorization and partitioning in the North Mountain thrust sheet, central Appalachians, USA. Journal of Structural Geology 13, 21–35.

Evans, M.A., Groshong Jr, R.H., 1994. A computer program for the Calcite Strain Gauge technique. Journal of Structural Geology 16, 277–281.

Evans, M.A., Elmore, R.D., Lewchuk, M.T., 2000. Examining the relationship between remagnetization and orogenic fluids: central Appalachians. Journal of Geochemical Exploration 69–70, 139–142.

Freeman, B., Ferguson, C.C., 1986. Deformation mechanism maps and micromechanics of rocks with distributed grain sizes. Journal of Geophysical Research 91, 3849–3860.

Frost, H.J., Ashby, M.F., 1982. Deformation Mechanism Maps, Pergamon Press, New York.

Fry, N., 1979. Random point distributions and strain measurement in rocks. Tectonophysics 60, 89–105.

Groshong, R.H. Jr, 1972. Strain calculated from twinning in calcite. Geological Society of America Bulletin 83, 2025–2038.

Groshong, R.H. Jr, 1974. Experimental test of the least squares strain gauge calculation using twinned calcite. Geological Society of America Bulletin 85, 1855–1864.

Groshong, R.H. Jr, 1988. Low temperature deformation mechanisms and their interpretation. Geological Society of America Bulletin 100, 1329–1360.

Groshong, R.H. Jr, Pfiffner, O.A., Pringle, L.R., 1984. Strain partitioning in the Helvetic thrust belt of eastern Switzerland from the leading edge to the internal zone. Journal of Structural Geology 6, 5–18.

Gwinn, V.E., 1964. Thin-skinned tectonics in the Plateau and western Valley and Ridge provinces of the central Appalachians. Geological Society of America Bulletin 75, 863–900.

Harris, J.H., van der Pluijm, B.A., 1998. Relative timing of calcite twinning strain and fold-thrust belt development; Hudson Valley fold-thrust belt, New York, USA. Journal of Structural Geology 20, 21–31.

Harrison, M.J., Onasch, C.M., 2000. Quantitative assessment of low-temperature deformation mechanisms in a folded quartz arenite, Valley and Ridge province, West Virginia. Tectonophysics 317, 73–91.

Head, J.W., 1974. Correlation and paleogeography of upper part of Helderberg Group (Lower Devonian) of central Appalachians. American Association of Petroleum Geologists Bulletin 58, 247–259.

Heald, M.T., 1956. Cementation of Simpson and St. Peter sandstones in parts of Oklahoma, Arkansas, and Missouri. Journal of Geology 64, 16–30.

Henry, B., 1989. Magnetic fabric and orientation tensor of minerals in rocks. Tectonophysics 165, 21–27.

Hirt, A.M., Lowrie, W., Pfiffner, O.A., 1986. A paleomagnetic study of the tectonically deformed red beds of the Lower Glarus Nappe Complex, eastern Switzerland. Tectonics 5, 723–732.

Hirt, A.M., Julivert, M., Soldevila, J., 2000. Magnetic fabric and

deformation in the Navia–Alto Sil slate belt, northwestern Spain. Tectonophysics 320, 1–16.

Housen, B.A., van der Pluijm, B.A., 1990. Chlorite control of correlations between strain and anisotropy of magnetic susceptibility. Physics of the Earth and Planetary Interiors 61, 315–323.

Housen, B.A., van der Pluijm, B.A., 1991. Slaty cleavage development and magnetic anisotropy fabrics. Journal of Geophysical Research 96, 9937–9946.

Housen, B.A., Richter, C., van der Pluijm, B.A., 1993. Composite magnetic anisotropy fabrics: experiments, numerical models, and implications for the quantification of rock fabrics. Tectonophysics 220, 1–12.

Hrouda, F., 1982. Magnetic anisotropy of rocks and its application in geology and geophysics. Geophysical Surveys 5, 37–82.

Hrouda, F., 1993. Theoretical models of magnetic anisotropy to strain relationship revisited. Physics of the Earth and Planetary Interiors 77, 237–249.

Hrouda, F., Jacko, S., Hanák, J., 1988. Parallel magnetic fabrics in metamorphic, granitoid, and sedimentary rocks of the Branisko and Čierna hora Mountains (E. Slovakia) and their tectonometamorphic control. Physics of the Earth and Planetary Interiors 51, 271–289.

Ihmlé, P.F., Hirt, A.M., Lowrie, W., 1989. Inverse magnetic fabric in deformed limestones of the Morcles nappe, Switzerland. Geophysical Research Letters 16, 1383–1386.

Imaz, A.G., Pocoví, A., Lago, M., Parés, J.M., 2000. Effect of lithostatic pressure and tectonic deformation on the magnetic fabric (anisotropy of magnetic susceptibility) in low grade metamorphic rocks. Journal of Geophysical Research 105, 21,305–21,317.

Jackson, M., 1991. Anisotropy of magnetic remanence: a brief review of mineralogical sources, physical origins, and geological applications, and comparison with susceptibility anisotropy. Pure and Applied Geophysics 136, 1–28.

Jackson, M., Tauxe, L., 1991. Anisotropy of magnetic susceptibility and remanence: developments in the characterization of tectonic, sedimentary, and igneous fabric. Geophysical Research Letters 29, 371–376.

Jackson, M., Sprowl, D., Ellwood, B., 1989. Anisotrophies of partial anhysteretic remanence and susceptibility in compacted black shales: grainsize- and composition-dependent magnetic fabric. Geophysical Research Letters 16, 1063–1066.

Jelínek, V., 1981. Characterization of magnetic fabric of rocks. Tectonophysics 79, T63–T67.

Kilsdonk, B., Wiltschko, D.V., 1988. Deformation mechanism in the southeastern ramp region of the Pine Mountain Block, Tennessee. Geological Society of America Bulletin 100, 653–664.

Kligfield, R.W., Lowrie, W., Pfiffner, O.A., 1982. Magnetic properties of deformed oolitic limestones from the Swiss Alps: the correlation of magnetic anisotropy and strain. Eclogea Geologica Helvetica Acta 75, 127–157.

Kulander, B.R., Dean, S.L., 1986. Structure and tectonics of central and southern Appalachian Valley and Ridge provinces, West Virginia and Virginia. American Association of Petroleum Geologists Bulletin 70, 1674–1684.

Lewchuk, M.T., Elmore, R.D., Evans, M.A., 2002. Remagnetization signature of Paleozoic sedimentary rocks from the Patterson Creek Mountain anticline in West Virginia. Physics and Chemistry of the Earth Parts A/B/C, 27, 1141–1156.

Lewchuk, M.T., Evans, M.A., Elmore, R.D., 2003. Synfolding remagnetization and deformation: results from Paleozoic sedimentary rocks in West Virginia. Geological Journal International, in press.

Lowrie, W., 1989. Magnetic analysis of rock fabric. In: James, D.E., (Ed.), The Encyclopedia of Solid Earth Geophysics, Van Nostrand Reinhold, Princeton, New Jersey, pp. 698–706.

Lüneburg, C.M., Lampert, S.A., Lebit, H.D., Hirt, A.M., Casey, M., Lowrie, W., 1999. Magnetic anisotropy, rock fabrics and finite strain in deformed sediments of SW Sardinia (Italy). Tectonophysics 307, 51–74.

Markley, M., Wojtal, S., 1996. Mesoscopic structure, strain, and volume loss in folded cover strata, Valley and Ridge province, Maryland. American Journal of Science 296, 23–57.

Marshak, S., Engelder, T., 1985. Development of cleavage in limestone of a fold-thrust belt in eastern New York. Journal of Structural Geology 7, 345–359.

Meyer, T.J., Dunne, W.M., 1990. Deformation of Helderberg limestones above the blind thrust system of the central Appalachians. Journal of Geology 98, 108–117.

Onasch, C.M., 1994. Assessing brittle volume-gain and pressure solution volume-loss processes in quartz arenite. Journal of Structural Geology 16, 519–530.

Owens, W.H., Bamford, D., 1976. Magnetic, seismic, and other anisotropic properties of rock fabrics. Philosophical Transactions of the Royal Society of London 283, 55–68.

Passchier, C.W., Trouw, R.A.J., 1996. Microtectonics, Springer-Verlag, New York.

Perry, W.J., 1978. Sequential deformation in the central Appalachians. American Journal of Science 278, 518–542.

Raj, R., 1982. Creep in polycrystalline aggregates by mass transport through a liquid phase. Journal of Geophysical Research 87, 4731–4739.

Raj, R., Ashby, M.F., 1971. Grain boundary sliding and diffusional creep. Metallurgical Transactions 2, 1113–1127.

Ramsay, J.G., Huber, M.I., 1983. The Techniques of Modern Structural Geology, Volume 1: Strain Analysis, Academic Press, New York.

Rochette, P., 1987. Magnetic susceptibility of the rock matrix related to magnetic fabric studies. Journal of Structural Geology 9, 1015–1020.

Rochette, P., 1988. Inverse magnetic fabric in carbonate-bearing rocks. Earth and Planetary Science Letters 90, 229–237.

Rochette, P., Jackson, M., Aubourg, C., 1992. Rock magnetism and the interpretation of anisotropy of magnetic susceptibility. Reviews of Geophysics 30, 209–226.

Rodgers, J., 1963. Mechanics of Appalachian foreland folding in Pennsylvania and West Virginia. American Association of Petroleum Geologists Bulletin 47, 1527–1536.

Rodgers, J., 1970. The Tectonics of the Appalachians, Wiley Interscience, New York.

Rutter, E.H., 1974. The influence of temperature, strain rate, and interstitial water in the experimental deformation of calcite rocks. Tectonophysics 22, 311–334.

Rutter, E.H., 1976. Kinetics of rock deformation by pressure solution. Philosophical Transactions of the Royal Society of London A283, 203–219.

Sacks, P.E., Secor, D.T. Jr, 1990. Kinematics of late Paleozoic continental collision between Laurentia and Gondwana. Science 250, 1702–1705.

Schmid, S.M., 1982a. Laboratory experiments on rheology and deformation mechanisms in calcite rocks and their application to studies in the field. Mitt. Geol. Inst. E.T.H. Univ. Zurich 241, 1–106.

Schmid, S.M., 1982b. Microfabric studies as indicators of deformation mechanisms and flow laws operative in mountain building. In: Hsu, K.J., (Ed.), Mountain Building Processes, Academic Press, London, pp. 95–110.

Schmid, S.M., Boland, J.N., Patterson, M.S., 1977. Superplastic flow in fine-grained limestone. Tectonophysics 43, 257–291.

Silbey, D.F., Blatt, H., 1976. Intergranular pressure solution and cementation of the Tuscarora orthoquartzite. Journal of Sedimentary Petrology 46, 881–896.

Smart, K.J., Dunne, W.M., Krieg, R.D., 1997. Roof response to emplacement of the Wills Mountain duplex: the roles of forethrusting and scales of deformation. Journal of Structural Geology 19, 1443–1459.

Spang, J.H., Groshong, R.H. Jr, 1981. Deformation mechanisms and strain history of a minor fold from the Appalachian Valley and Ridge province. Tectonophysics 72, 323–342.

Stamatakos, J., Kodama, K.P., 1991a. The effects of grain-scale deformation on the Bloomsburg Formation Pole. Journal of Geophysical Research 96, 17,919–17,933.

Stamatakos, J., Kodama, K.P., 1991b. Flexural flow folding and the paleomagnetic fold test: an example of strain reorientation of remanence in the Mauch Chunk Formation. Tectonics 10, 807–819.

Stockdale, P.B., 1926. The stratigraphic significance of solution in rocks. Journal of Geology 34, 399–414.

Sun, W., Jackson, M., Craddock, J.P., 1993. Relationship between remagnetization, magnetic fabric, and deformation in Paleozoic carbonates. Tectonophysics 221, 361–366.

Tarling, D.H., Hrouda, F., 1993. The Magnetic Anisotropy of Rocks, Chapman and Hall, London.

Wanless, H.R., 1979. Limestone response to stress: pressure solution and dolomitization. Journal of Sedimentary Petrology 49, 437–462.

Wilson, T.H., Shumaker, R.C., 1992. Broadtop thrust sheet: an extensive blind thrust in the central Appalachians. American Association of Petroleum Geologists Bulletin 76, 1310–1324.

Wu, S., 1989. Strain partitioning and deformation mode analysis of the normal faults at Red Mountain, Birmingham, Alabama. Tectonophysics 170, 171–182.